THESIS FOR THE DEGREE OF LICENTIATE OF ENGINEERING

in

Thermo and Fluid Dynamics

Plasma Arc Welding Simulation with OpenFOAM

by

MARGARITA SASS-TISOVSKAYA

Department of Applied Mechanics
CHALMERS UNIVERSITY OF TECHNOLOGY
Göteborg, Sweden, 2009

Plasma Arc Welding Simulation with OpenFOAM
MARGARITA SASS-TISOVSKAYA

THESIS FOR LICENTIATE OF ENGINEERING no. 2009:10
ISSN 1652-8565

Department of Applied Mechanics
Chalmers University of Technology
SE-412 96 Göteborg
Sweden
Telephone +46-(0)31-7721000

This document was typeset using LaTeX

Printed at Chalmers Reproservice
Göteborg, Sweden, 2009

Abstract

A simulation tool that is valid within the field of tandem arc welding (unsteady, three dimensional thermal plasma flow) has been developed, based on the open source CFD package OpenFOAM. The validation of the electromagnetic part of the solver has been done separately using a problem with a known solution. A good agreement between the numerical and analytical solutions was obtained. Different boundary conditions on the magnetic potential vector have been tested. Based on these tests, the appropriate boundary conditions were chosen for the case representing a transferred arc configuration. The complete simulation tool was validated using a tungsten inert gas single arc problem. Two representations of the magnetic field have been tested, based on the electric and magnetic potentials, respectively. Qualitatively, both approaches agreed well with the results found in the literature. However, quantitatively a deviation in the results was observed in the near cathode region.

Acknowledgments

First and foremost I wish to express my sincere gratitude to my advisors, Isabelle Choquet and Håkan Nilsson. Your knowledge, assistance, involvement and infinite patience made this work a reality and I deeply appreciate that. It has been a privilege and pleasure being your student. A very special thanks goes to Lars Davidson, my examiner. He has always showed a never failing enthusiasm for my work and has been a source of constant encouragement.

I also want to extend my thanks to all my colleagues and friends at Högskolan Väst, present and former, for sharing both study and fun time together.

Finally, I want to thank my parents and my sister, for all their care, support and love. Last but not least, I would like to thank my dear husband, Alexei, from the depth of my heart, for his never ending love, for his endless support, understanding and sacrifices during all these years.

I also want to thank the partners of this project supported by the KK-foundation: ESAB, Volvo Construction Equipment, SSAB and Migatronic. All financial supporters are gratefully acknowledged.

Preface

The present work is divided in four chapters.

Chapter 1 presents the motivation and goals of the work. This is followed by a description of the tandem arc welding process and the essential elements of a single arc formation. A brief summary of related work by other authors is also included.

Chapter 2 covers the main assumptions used in the formulation of the mathematical model. This is followed by a discussion on the modeling of the thermodynamic and transport properties. Finally, the governing equations used in the current work are summarized.

Chapter 3 presents a brief introduction to the used software and implementation details. The proposed model and solution procedure are validated with the help of two test cases. The first test case covers the validation of the electromagnetic part of the model and tests the boundary conditions on the magnetic potential vector. In the second test case, validation of the transferred arc configuration is carried out. In addition, the effects of two different ways of calculating electromagnetic field on the arc are studied.

Finally, in Chapter 4 the work is summarized, conclusion are drawn, and future work is suggested.

Some additional details on the modeling of the thermodynamic and transport properties are given in the Appendix *A*. A short description of the finite volume method is presented in the Appendix *B*. The discretization of the transport equation is explained term by term. The segregated approach for the coupled system of differential equations that is used in this study is described, and the solution procedure for transient arc plasma model is summarized.

Contents

Abstract **3**

Acknowledgements **5**

Preface **7**

Contents **8**

1 Introduction **11**
1.1 Motivation of the study 11
1.2 TIG welding arc process 12
1.3 Single arc physics 13
1.4 Historical background 15

2 Model of the thermal arc plasma column **19**
2.1 Magnetohydrodynamic model 19
2.1.1 Modeling the flow of the conduction plasma fluid . . 19
2.1.2 Modeling the energy transport within the plasma . . 20
2.1.3 Modeling the electromagnetic phenomena within the plasma 21
2.1.4 Summary of the electromagnetic equations used in the model 26
2.1.5 Derivation of the potential formulation of the model 26
2.1.6 Calculation of the magnetic field for 2D axi-symmetric problems 27
2.2 Thermodynamic and transport properties 28
2.2.1 Composition of a simple argon gas 28
2.2.2 Summary of the thermal plasma properties 30
2.3 Summary of arc column modeling 34

3 Implementation and validation **37**
3.1 Development in OpenFOAM 37
3.2 Validation of the electromagnetic part 40
3.2.1 Infinite electric rod 40
3.2.2 Description of the simulations 41

3.2.3 Results and validation 43
3.2.4 Test of boundary conditions 46
3.3 Transferred arc configuration – 2D axi-symmetric test case . 49
3.3.1 Problem description 49
3.3.2 Description of the cases 50
3.3.3 Numerical results 53

4 Conclusions and future work **57**

A Details on the thermodynamic and transport properties **65**
A.1 Density 65
A.2 Dynamic viscosity 67
A.3 Thermal conductivity 69
A.4 Enthalpy and specific heat 72
A.5 Plasma radiation 73

B Numerical solution and algorithm **77**
B.1 Discretization of the transport equation 77
B.1.1 Temporal derivative 78
B.1.2 Convection term 78
B.1.3 Diffusion term 79
B.1.4 Source term 79
B.1.5 Boundary conditions 80
B.1.6 Solution of the linear equation system 80
B.2 Solution algorithm for the pressure-velocity coupling 81
B.2.1 Derivation of the pressure equation 81
B.2.2 Assembling the conservative fluxes 82
B.2.3 The SIMPLE algorithm 83
B.2.4 Under-relaxation procedure 84
B.2.5 Solution procedure for the system 84

Chapter 1

Introduction

1.1 Motivation of the study

Arc welding is a technique to melt and join different materials, that is widely used in the industry. Nowadays, various arc welding methods are available. Tandem arc welding is one type of welding method, whose main characteristic is the use of a double heat source and the presence of two electric arcs, see Fig. 1.1. The electrical circuits can either be dependent or independent in terms of the power source, but each with its own wire. The wires act as electrodes and provide the filler material. These two wires are fed through two separate contact tubes. The two contact tubes are contained in a common torch body, and surrounded by a common shielding gas. These two wires may differ in diameter and composition when two independent electrical circuits are used since parameters such as the arc voltage can be set independently on each wire. The arcs can have different functions: the leading arc heats both the wire and the base metal to form a molten pool, whereas the trailing arc melts the second wire to fill up the pool and smooth the surface of the weld. The type of arc interaction, the amount of heat transferred to the work piece, and the pressure force applied on the molten pool depend on electrical, material and geometrical parameters (such as tip shape, angle and distance between tips).

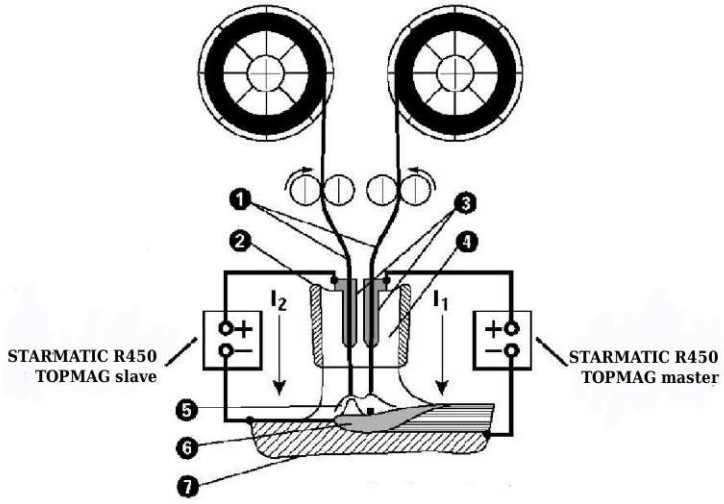

Figure 1.1: A sketch of tandem arc welding. The following notation is used: 1-wire; 2-gas nozzle; 3-contact tubes; 4-shielding gas; 5-electric arc; 6-molten pool; 7-part to be welded (*www.saairliquide.com*).

.

Tandem arc welding results in highly increased deposition efficiency. However, the process stability is still a critical issue. The arcs may indeed blow up while passing close to, or turning around, a metallic piece. A better understanding and control of the process is thus needed to extend its applicability. The operating conditions are extreme, with a temperature rise from room temperature to about 25 000K, which corresponds to plasma fluid, within a few millimeters. The imposed electric field and induced magnetic field are driving forces for the plasma flow. The experimental characterization of an electric arc is a difficult task that needs to be supported by numerical simulations.

Therefore, the aim of this work was to develop a simulation tool valid within the frame of tandem arcs (unsteady, three dimensional thermal plasma flow). The model is implemented in the open-source CFD software OpenFOAM (*www.openfoam.org*). For validation purposes, the simulation tool is initially applied to a single welding arc case. In addition, since the droplet and welding pool dynamics are not yet accounted for at the moment, a tungsten inert gas (TIG) welding application has been chosen as the main reference case.

1.2 TIG welding arc process

There are different types most common welding techniques that employ a single arc to heat and fuze the metals. These are the Gas Metal Arc welding, the Gas Tungsten Arc welding (GTAW) and the Shielded Metal Arc

welding. This work considers only the GTAW, also known as tungsten inert gas (TIG) welding. This arc welding process uses a non-consumable tungsten electrode to produce the weld. The filler material is in this case provided by a separate filler rod. The weld area is protected from atmospheric contamination by a shielding gas.

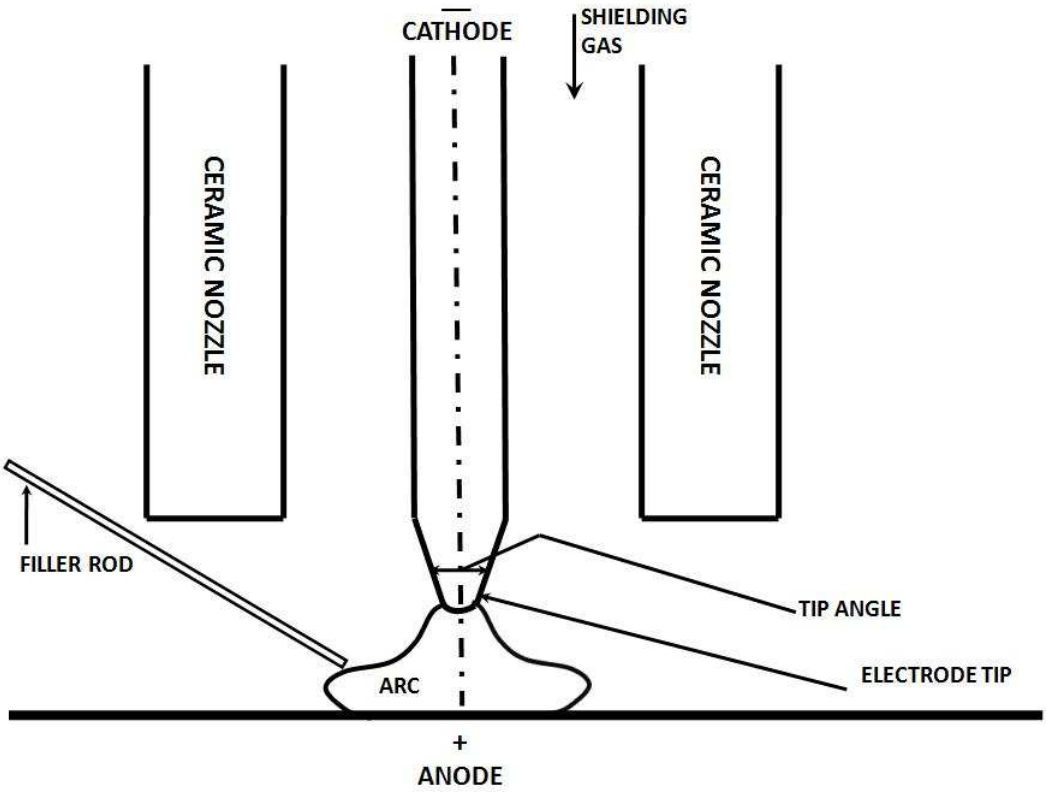

Figure 1.2: A typical sketch of the TIG welding.

A schematic sketch of the TIG welding process is shown in Fig. 1.2. The cathode is a tungsten electrode. This electrode is surrounded by a ceramic nozzle, whose function is to direct the shielding gas towards the surface being welded, the anode. The filler material is fed through the filler rod.

The complete welding process is complex in nature as it includes various phenomena such as multiphase flow in the plasma arc and the weld pool, droplet and welding pool dynamics, and metal transfer. The present work mainly focuses on modeling the plasma arc column. The basic assumptions, that are generally accepted in welding arc modeling, are presented and discussed in Chapter 2.

1.3 Single arc physics

Electric discharges can be formed by applying a voltage between two electrodes. In the present work, the specific electric discharge called electric

arc is considered. The main characteristic features of an electric arc are: a high current (30 A- 30kA), a low voltage between electrodes (10-100V), a power level per unit length larger than 1 kW/cm, a moderate ionization degree with an electron density within the range of 10^5 to 10^9 electrons per cm^3, and atmospheric or even larger gas pressure (0.1-100 atm) [48]. This results in a very high temperature, capable of melting or vaporizing most materials.

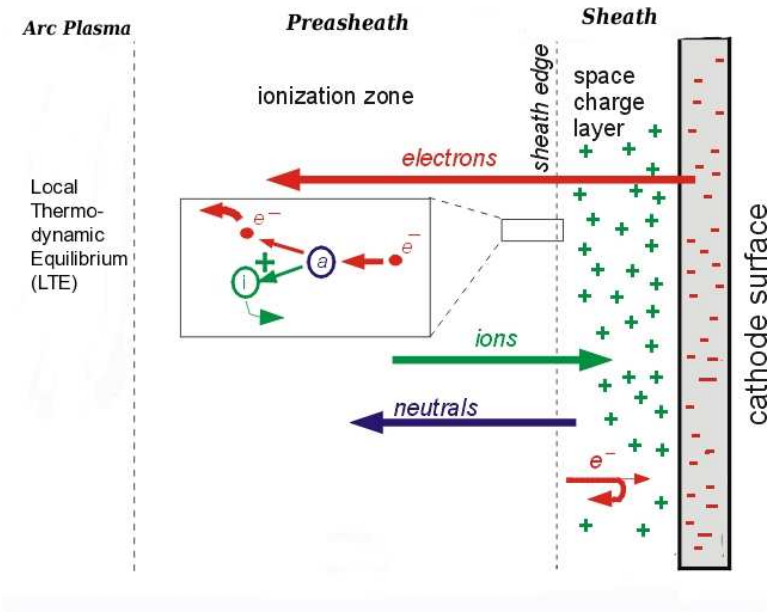

Figure 1.3: Sketch of the zones near an electron emitting cathode surface [5].

It is generally considered that an electric arc consists of three major parts: the thermal plasma column, the cathode and anode layer [49], see Fig 1.3. The cathode layer is subdivided in two zones: the sheath (or space charge layer) and the presheath (or ionization zone). In the sheath the conduction process switches: from metallic of the cathode surface to gaseous in the plasma. The sheath zone is very thin, roughly of the order of one electron mean free path. Electrons are thus almost collisionless in the layer characterized by the absence of thermal equilibrium. This zone is mainly made of positive ions, thus its name of space charge layer. These ions lead to thermionic emission of electrons as they collide with the cathode surface. They also build up a potential fall that accelerates the emitted electrons towards the ionization zone.

Within the presheath zone, the energy transfer between the emitted electrons and the heavy particles takes place during collisions inducing ionization, thus its name of ionization zone. The thickness of this zone is characterized by the recombination length and is much thicker than the

sheath[1]. This zone is considered to be in partial thermal equilibrium[2] and quasi-neutral. It is followed by the plasma column that represents the main body of the arc. In the considered case, the plasma column is of the order of 10^{-2} m. This region is in local thermal equilibrium (LTE),[3] free of space charge, and both ionization and recombination take place.

Finally, the anode layer is subdivided in the same manner as the cathode, though with a different distribution of electric potential [49].

Due to the passage of the electric current between the electrodes a magnetic field is induced. As a result of the interaction between the magnetic flux density of the magnetic field and the current density, the Lorentz force is produced that acts as a major source term in the momentum equations governing the plasma flow. In the particular case of an axi-symmetric configuration this force is aligned with the radial direction of the arc and points towards the symmetry axis. As the distance from the cathode increases, the electromagnetic force decreases in intensity. Due to the strong variation in the Lorentz force, a large pressure gradient is formed just below the cathode surface. As a result, a high-velocity plasma (or ionized shielding gas) jet is directed from the cathode towards the anode surface. Upon reaching the stagnation zone near the anode surface the jet is deflected [8]. From the stagnation zone, the jet flows radially outwards, producing a well-known bell-shape arc.

1.4 Historical background

Investigations for understanding and modeling electric arcs started with the first detection of the arc phenomena, in the beginning of 19th century [47]. Under the assumption of LTE, a hydrodynamical model for the plasma arc column can be derived from the conservation of momentum, mass and energy, supplemented with an equation of state. In order to account for the electromagnetical effects, the above hydrodynamical model has to be completed with the Maxwell's equations (usually in a simplified form). The interaction between the flow and the electromagnetic field is complex. The strong dependence of the flow on the thermophysical properties of the plasma is also present. As a result, the analytical solution of the complete system of equations is only possible after introducing a number of constraining simplifications and assumptions, therefore signif-

[1] In the considered case of electric arc, the recombination length is larger than the mean free path by about two orders of magnitude, and larger than the Debye length by about one order of magnitude

[2] The electron temperature is almost twice larger than the temperature of the heavy particles (ions and neutrals)

[3] The LTE assumption implies that the temperature of the electrons and the heavy particles are the same

icantly reducing the models applicability. As a result, until recently, the technology of electric arc was mainly based on experimental trial and error rather than theoretical understanding and prediction.

An alternative approach for the solution of the complete system of equations is to perform numerical simulations. The first work that considered the heat transfer and fluid flow in the arc column with coupled electromagnetic forces was done by Hsu *et al.* [11]. In this work, a steady, 2-dimensional model of 10 mm long free burning arc[4] was considered.

The work by Hsu *et al.* was continued by McKelliget and Szekely [9], who made a refined representation of the heat and current flux density at the electrode surface. Both of these studies dealt with a tungsten electrode with a known current density, a water-cooled anode surface, and a flat/stepwise approximation of the electrode tip.

In the attempt to confirm the validity of the LTE assumption, Hsu and Pfender [45] used a two-temperature model [5]. Their results indicated that the LTE should be a valid assumption in the arc plasma, especially in the regions where the temperature is greater than 10000 K. Therefore the ordinary one-temperature model should be sufficient.

Over time, various two-dimensional numerical models of increased sophistication have emerged. Choo *et al.* [35], Lee and Na [36], Goodarzi *et al.* [37], Lowke *et al.* [38] have developed numerical models with improved capabilities. These improvements included a more accurate prediction of the electrode temperature distribution [35], the introduction of various aspects of electrode geometry in the calculation domain [36]-[37], and different shielding gas (mixture of argon and hydrogen) [38]. The majority of these studies considered the case of axi-symmetric flows and the main investigation was concentrated on the interaction between the arc and the electrodes. The results confirmed that the boundary conditions on the electrodes have a profound effect on the arc discharge.

In the context of the present work, it is also important to mention the work of Tsai and Kou [24]. In their study a steady two-dimensional model of the transferred arc[6] has been introduced. This work differs from the previous ones in that it considers an arc length that corresponds to actual welding applications. It further accounts for the presence of the shielding gaz nozzle and deals with various electrode tip geometries. As in the previous studies, the sensitivity of the heat transfer and plasma column

[4] A free burning arc is a specific arc configuration. As the name implies, no external stabilizing mechanism is applied on the arc [21]. The flow of gas in a free burning arc is only caused by the electromagnetic forces generated by the arc itself.

[5] In the partial thermal equilibrium case, two coupled conservation equations for energy are needed [45], one for the electrons and one for the heavy species (ions and neutrals).

[6] In the case of the transferred arc workpiece is an electrode.

flow to the current distribution was reported. Compared to the previously considered long arcs, a higher width to height ratio of the bell shaped arc was observed. Finally, the effects of the electrode tip geometry on the arc shape was reported and compared with experimental observations.

Some physical aspects of the arc problem, such as the influence of a non-uniform gas injection and geometry asymmetry cannot be considered by the two dimensional models. Therefore, a complete three-dimensional model is then required. Recently, a number of three-dimensional models have been reported in the literature. The first of these models were still constraint by the symmetry assumption. For example, Delandore *et al.*[42] studied a symmetric transferred arc with an argon shielding gas. Also the arc fluctuations were considered, but due to the symmetry assumptions these fluctuation were constrained to two horizontal planes (corresponding to the cathode and the anode surfaces).

Further development of the model was concentrated on relaxing the symmetry constraint, considering a 3D unsteady model of the free burning arc [16]. No symmetry assumption was set. But due to computational reasons the complete geometry was simplified to two parallel planes, including the cathode and the anode (represented by two predefined conducting circular regions). The results were compared with the work of Hsu *et al.* [11]. The comparison was done only along the axis of symmetry and significant differences were reported.

The study of a free burning arc by Freton *et al.* [17] presented a more detailed 3D geometry. First, a 2D configuration was presented and compared with the case studied by Hsu *et al.* [11] in order to validate the model. Then the results of the 2D free burning arc calculation was compared with a complete 3D calculation done using the same boundary conditions. As expected, the results showed no significant difference, and it was concluded that a 2D model can still be an efficient and accurate representation for an axisymmetric problem. Then the model was applied to a transferred arc configuration with a three-dimensional effect: a vortex injection. In the case of a significant mass flow rate injection of the shielding gas a noticeable difference between 2D and 3D simulation results was observed. The 2D approximation was not considered acceptable outside of the arc core region.

To summarize:

- Most of the arc models found in the literature consider a laminar flow regime. This is explained by the fact that the characteristic Reynolds number is usually considered to be too low for the turbulence to appear (a threshold value of 100000 is usually referred to, when a transition to turbulence in a free jet occurs [9]). But flow instabilities could also be caused by the electromagnetic forces, as underlines in

[25].

- Many authors chose to concentrate their efforts on different aspects of the electric arc than those mentioned above. That is Lowke [40] and Ushio *et al.* [39] contributed by a study of the electrode sheaths of the anode and cathode surfaces, making it possible to avoid the assumption of a specified current density distribution. Tanaka *et al.* [41] presented a first model that considered simultaneously both the arc region and the weld pool. Hu and Tsai [43] further developed the coupled arc-pool approach. They studied the effects of different current profiles on the plasma generation, weld pool and droplet dynamics.

Unfortunately, no published literature has been found on numerical simulation of tandem arc welding.

It is the purpose of the present work to develop a comprehensive simulation tool for tandem arc welding. Due to the asymmetry of the problem, a three-dimensional model is required. A simulation tool for a three-dimensional transferred arc model has been implemented and being validated. The model is based on the LTE assumption, it accounts for the unsteady effects, and the strong dependence of the flow on the thermophysical properties of the plasma. The implementation is tested for a 3D single transferred arc. For the sake of generality, both the shielding gas nozzle and the surface of the conical electrode tip geometry are included in the computational domain. In addition, a 2 mm arc length corresponding to an actual welding application is considered. The results for the transferred arc simulation are compared with those of Tsai *et al.* [24]. Characteristic values of the considered arc configuration are compiled in Table 1.1. These values are used in Chapter 2 for the dimensional analysis.

T_c[K]	V_c [m/s]	t_c [s]	L_c [m]	R_c [m]
$2 \cdot 10^4$	200	10^{-5}	$2 \cdot 10^{-3}$	$4.5 \cdot 10^{-3}$

Table 1.1: Characteristic parameters.

.

Here T_c is the characteristic temperature that corresponds to the maximum arc temperature. The characteristic velocity V_c represents the maximum speed of the shielding gas jet (located under the cathode). The characteristic arc length L_c represents the distance between cathode and anode surface, and R_c the characteristic arc radius. The arc radius was evaluated at a distance of 10^{-3} m from the anode surface using the $T = 11 \cdot 10^3$ K isotherm as a boundary for delimiting the plasma column. The characteristic time t_c was evaluated as a ratio of characteristic length to characteristic speed.

Chapter 2

Model of the thermal arc plasma column

2.1 Magnetohydrodynamic model

In this chapter, the governing equations for a three-dimensional welding arc are presented. As already underlined in the previous chapter, the quantities (such as the Reynolds number or the Debye wavelength) used below to justify possible simplifications are evaluated based on the TIG test case of Tsai *et al.* [24]. A special attention is paid to the modeling of the thermodynamic and transport properties of the plasma column. Radiation effects are also discussed. Finally the mathematical model is summarized together with the assumptions made.

2.1.1 Modeling the flow of the conduction plasma fluid

In this section, the flow of the plasma column that is under LTE assumption is considered. In the present case, the Reynolds number, $Re \approx 377$, is not small but well below the critical value for turbulent flow ($Re_c \approx 10000$) [24]. The laminar flow of a heat conducting viscous fluid, which is mechanically incompressible ($Ma \approx 0.01$) but thermally expansible (the density depends of the temperature), is governed by the following set of equations:

- Conservation of mass

$$\frac{\partial}{\partial t}\rho + \nabla \cdot (\rho U) = 0 \tag{2.1}$$

  where U is the velocity of the flow and ρ is the density that depends here on the temperature. The temperature dependence of ρ is discussed in Section 2.2.

- Conservation of momentum :

$$\frac{\partial}{\partial t}(\rho U) + \nabla \cdot (\rho U U) - \nabla \cdot [\mu(\nabla U + (\nabla U)^T) - \frac{2}{3}\mu(\nabla \cdot U)I] = -\nabla p + \underbrace{j \times B}_{\text{Lorenz force}} \tag{2.2}$$

where j is the electric current density, B is the magnetic field and the stress tensor satisfies Newton's law of viscosity. The dynamic fluid viscosity μ depends here on the temperature. More details about the dynamic viscosity are given in Section 2.2. In the equation above, p is the static pressure and I is the unit tensor.

2.1.2 Modeling the energy transport within the plasma

The energy transport within the plasma is governed by the following enthalpy conservation equation:

$$\frac{\partial}{\partial t}(\rho h) + \nabla \cdot (\rho U h) - h\nabla \cdot \rho U + \nabla \cdot q = \nabla \cdot (Up) - p\nabla \cdot U + \underbrace{j \cdot E}_{\text{Joule heating}} - \underbrace{4\pi\epsilon_N}_{\text{Radiation loss}} + \underbrace{\nabla \cdot \left(\frac{5k_b j}{2ec_p}h\right)}_{\text{Transport of the electron enthalpy}} \tag{2.3}$$

where h is the enthalpy, E the electric field, ϵ_N the net emission coefficient that is described in Section 2.2 , k_b the Boltzmann constant and e the electric charge. The heat conduction is given by Fourier's law $q = -\alpha\nabla h$ where α is the thermal diffusivity given by

$$\alpha = \frac{\kappa(T)}{\rho c_p(T)}.$$

Here κ is the temperature dependent thermal conductivity, see Section 2.2.

The temperature is defined from the specific enthalpy using the definition of the specific heat capacity at constant pressure

$$c_p(T) = \left(\frac{\partial h}{\partial T}\right)_p$$

where c_p is a function of the temperature, see Section 2.2.

2.1.3 Modeling the electromagnetic phenomena within the plasma

in arc welding, once the arc is established, the presence of an imposed electric field between the cathode and the anode causes the passage of an electric current through the ionized plasma region. The electric current gives rise to an induced magnetic field. The magnetic field interacts with the current transferring momentum to the gas, which is accelerated towards the anode in the form of the characteristic cathode jet. Due to the electrical resistance of the plasma, the Joule heating produced by the current maintains the plasma in an ionized state and provides the heating mechanism for the welding process.

This electromagnetic phenomena is modeled with the help of Maxwell's equations:

- Faraday's law:

$$\frac{\partial B}{\partial t} = -\nabla \times E \tag{2.4}$$

- Ampere's law:

$$\epsilon\mu\frac{\partial E}{\partial t} = \nabla \times B - \mu j \tag{2.5}$$

- Gauss' law (electric):

$$\nabla \cdot E = \frac{q_{tot}}{\epsilon} \tag{2.6}$$

- Gauss' law (magnetic):

$$\nabla \cdot B = 0 \tag{2.7}$$

where q_{tot} is the total electric charge, μ denotes here the permeability and ϵ the permittivity of the medium.

These four Maxwell equations are supplemented by the following equations:

- Conservation of the electric charge:

$$\frac{\partial q_{tot}}{\partial t} + \nabla \cdot j = 0 \tag{2.8}$$

- Ohm's law:

$$j = \sigma_m\{\underbrace{E}_{\text{Electric current}} + \underbrace{U \times B}_{\text{Induction current}} - \underbrace{\frac{1}{n_e} j \times B}_{\text{Hall current}}\} \tag{2.9}$$

where n_e is the electron density.

The permeability is described with two parameters [10]:

$$\mu = \mu_0(1 + \chi_m) \approx \mu_0$$

where χ_m is the magnetic susceptibility and μ_0 is the permeability of free space ($4\pi \times 10^{-7}\ N/A^2$). The magnetic susceptibility is a non-dimensional constant determined by the physical properties of the magnetic material. In the present work an argon gas is used as shielding gas. Its magnetic susceptibility is of the order of 10^{-9}. The magnetic permeability is thus equal to the magnetic permeability of vacuum.

The permittivity of the medium is expressed as

$$\epsilon = \epsilon_0(1 + \chi_e) \approx \epsilon_0$$

with ϵ_0 denoting the permittivity of free space ($8.85 \cdot 10^{-12}\ A^2 s^4 kg^{-1} m^{-3}$) and χ_e the electric susceptibility. For an argon gas, the value of the electric susceptibility can be neglected [10].

Due to the nature of the considered problem, the Maxwell equations can be simplified based on the following assumptions:

1. **Electro-neutrality**

   As mentioned in Section 1.3, in the plasma arc column, the mean free path[7] of an electron (of the order of $\lambda_e = 10^{-6}m$ [49]) is much larger then the Debye wavelength[8] (of the order of $\lambda_D = 10^{-8}m$ [49]). The Debye wavelength itself is very small compared to the macroscopic scale used to model the plasma. It can thus be considered that each volume element (i.e mesh cell) is *electrically neutral* at the macroscopic scale (the total electric charge is zero) [28].

   Under the assumption of electro-neutrality, Gauss' law for electric field 2.6 and the conservation equation for the electric charge 2.8 can respectively be simplified to :

   $$\nabla \cdot E = 0 \tag{2.10}$$

   and

   $$\nabla \cdot j = 0. \tag{2.11}$$

2. **Quasi-steady electromagnetic phenomena**

   Upon the application of the rotational operator to Faraday's law 2.4, the following equation is obtained

   $$\nabla \times (\nabla \times E) = -\nabla \times (\frac{\partial B}{\partial t}). \tag{2.12}$$

[7] The *"mean free path"* is the average distance that a particle travels between two collisions

[8] The *"Debye wavelength* represents the screening length of a particle before it gets influenced by the electro-magnetic field, $\alpha_D = \sqrt{\frac{\epsilon_0 k_b T_e}{n_e e^2}}$

The right hand side can be rewritten using Amper's law with $\mu = \mu_0$ and $\epsilon = \epsilon_0$, as

$$\nabla \times (\nabla \times E) = -\frac{\partial}{\partial t}(\mu_0 j + \epsilon_0 \mu_0 \frac{\partial E}{\partial t}). \tag{2.13}$$

Using the properties of the $\nabla \times (\nabla \times)$ operator[9] and Eq. 2.10, the following equation is obtained

$$\Delta E = \mu_0 \frac{\partial j}{\partial t} + \epsilon_0 \mu_0 \frac{\partial^2 E}{\partial t^2}. \tag{2.14}$$

A dimensional analysis is now done, as described in [28] in the different content of atmospheric plasma spraying, comparing the left hand side term to the second term on the right hand side of Eq. 2.14, the following ratio is obtained

$$\frac{\mid \epsilon_0 \mu_0 \frac{\partial^2 E}{\partial t^2} \mid}{\mid \Delta E \mid} \approx \frac{\epsilon_0 \mu_0 \frac{E_c}{t_c^2}}{\frac{E_c}{L_C^2}} = \frac{\epsilon_0 \mu_0 L_c^2}{t_c^2}$$

Here L_c and t_c are the characteristic length and time, given in Table 1.1. For the characteristic length of $2 \cdot 10^{-3}$ m and the characteristic time of 10^{-5} s the above ratio yields a value of $4.4 \cdot 10^{-18}$, implying that

$$\mid \epsilon_0 \mu_0 \frac{\partial^2 E}{\partial t^2} \mid << \mid \Delta E \mid .$$

As a result, the second temporal derivative can be omitted and Eq. 2.14 is simplified to

$$\Delta E = \mu_0 \frac{\partial j}{\partial t}.$$

Combining this result with Eqs. 2.12 and 2.10, the following equation is deduced

$$\nabla \times \frac{\partial B}{\partial t} = \mu_0 \frac{\partial j}{\partial t}.$$

The convection current can be neglected compared to the conduction current in Ampere's law. This simplification is called the quasi-steady assumption. Ampere's law is then reduced to the following equation

$$\nabla \times B = \mu_0 j. \tag{2.15}$$

3. **The magneto-hydrodynamic approach is valid**

   Let us first evaluate the Hall parameter to determine if the Hall current can be neglected. For an arc current of 200 A and an arc column

[9] For a general vector a the following identity holds: $\nabla \times (\nabla \times a) = \nabla(\nabla \cdot a) - \Delta a$

with a characteristic radius of 0.0045 m (see Table 1.1), the characteristic magnetic field is, according to Eq. 2.15, of the order of $B_c = 10^{-4}$ T. The corresponding Larmor frequency, that represents the precession frequency of electrons in a magnetic field B_c, is expressed as

$$\omega_e = \frac{eB_c}{m_e} \approx 2 \cdot 10^8 \text{ Hz}$$

where m_e is the electron mass.

The average collision frequency of electrons with other particles is derived from

$$\nu_{e,\beta} = \frac{n_e e^2}{m_e \sigma_c} = 2,8 \cdot 10^{11} \text{ Hz} .$$

where the characteristic electrical conductivity of the media $\sigma_c \approx 10^4$ $[A \cdot V^{-1} m^{-1}]$ and the characteristic electron density $n_e \approx 10^{23}$ $[m^{-3}]$ are taken for the temperature value of $T_c = 2 \cdot 10^4$ K (see Table 1.1).

The Hall parameter is defined as

$$\beta_c = \frac{\omega_e}{\nu_{e,\beta}} \approx 10^{-3}.$$

Under the above conditions, β_c is much less than unity. This means that the motion of the charged particles under the action of the electromagnetic field is stopped because of collisions with other particles. Due to this fact the Hall current can be neglected in Eq. 2.9.

The general Ohm's law 2.9 can then be simplified to the following form

$$j = \sigma_m (E + U \times B) \tag{2.16}$$

In a second step let us evaluate the magnetic Reynolds number to determine if the induction current can also be neglected. Combining Eq. 2.16 and Eq. 2.15 yields

$$\frac{1}{\mu_0 \sigma} \nabla \times B = E + U \times B \tag{2.17}$$

The rotational operator applied to this last relation leads to

$$\nabla \times (\frac{1}{\mu_0 \sigma_m} \nabla \times B) = \nabla \times E + \nabla \times (U \times B) \tag{2.18}$$

Using Faraday's law 2.4, an equation similar to a transport equation for the magnetic field is obtained

$$\frac{\partial B}{\partial t} = \nabla \times (U \times B) - \nabla \times (\frac{1}{\mu_0 \sigma_m} \nabla \times B) \tag{2.19}$$

It relates the current induced by the time-variations of the the magnetic field, $\frac{\partial B}{\partial t}$, to the current induced by the fluid motion, $\nabla \times (U \times B)$ and the conduction current, $\nabla \times (\frac{1}{\mu_0 \sigma_m} \nabla \times B)$.

A dimensionless study of this equation, as was proposed by Baudry [28], can be done using the screening dimensionless parameter[9] R_ω and the magnetic Reynolds number [10] R_{mag} .

A comparison of the current induced by the flow motion and the conduction current yields the following relation

$$\frac{\mid \mu_0 \sigma_c \nabla \times (U \times B) \mid}{\mid \nabla \times (\nabla \times B) \mid} \approx \frac{\mu_0 \sigma_c \frac{1}{L_c} V_c B_c}{\frac{1}{L_c} \frac{1}{L_c} B_c} = \mu_0 \sigma_c L_c V_c = R_{mag} \qquad (2.20)$$

with the characteristic parameters previously defined in Table 1.1. The magnetic Reynolds number is then approximately equal to 0.01. As a result, the induction current is negligible compared to the conduction current. Then the transport equation for the magnetic field Eq. 2.19, and the simplified Ohm's law Eq. 2.16, respectively reduce to

$$\frac{\partial B}{\partial t} = -\nabla \times \left(\frac{1}{\mu_0 \sigma_m} \nabla \times B \right) \qquad (2.21)$$

and

$$j = \sigma_m E.$$

Finally let us evaluate the screening parameter to determine if the time-variation of the magnetic field can be neglected.

Comparing now the time-variation of the magnetic field to the conduction current, the following relation is obtained

$$\frac{\mid \mu_0 \sigma_c \frac{\partial B}{\partial t} \mid}{\mid \nabla \times (\nabla \times B) \mid} \approx \frac{\mu_0 \sigma_c \frac{B_c}{t_c}}{\frac{1}{L_c} \frac{1}{L_c} B_c} = \frac{\mu_0 \sigma_c L_c^2}{t_c} = R_\omega$$

The characteristic values of Table 1.1 led a screening parameter R_ω of 0.03.

The screening parameter is less than one, implying that the current induced by the time-variation of the magnetic field is negligible compared to the conduction current. The criteria for steady state regime is thus satisfied, and Faraday's law can be reduced to

$$\nabla \times E = 0.$$

[9] The screening parameter is defined as the ratio of the time-variation of the magnetic field to the conduction current.

[10] The magnetic Reynolds number gives an estimate of the effects of magnetic advection to magnetic diffusion.

2.1.4 Summary of the electromagnetic equations used in the model

Taking into account the assumptions previously discussed, the electromagnetic equations are written in the following form

$$\nabla \cdot j = 0, \tag{2.22}$$
$$\nabla \cdot B = 0, \tag{2.23}$$
$$\nabla \cdot E = 0, \tag{2.24}$$
$$\nabla \times B = \mu_0 j, \tag{2.25}$$
$$\nabla \times E = 0, \tag{2.26}$$
$$j = \sigma_m E. \tag{2.27}$$

Combining the set of Eqs 2.22-2.27, the *potential* formulation of the electromagnetic field is now derived.

2.1.5 Derivation of the potential formulation of the model

In this section a derivation of the potential formulation of Maxwell's equations is done. The scalar electric potential ϕ and the vector potential A are first introduced. These potential functions are arbitrary, but they are required to satisfy Maxwell's equations. The derivation is based on two fundamental vector identities

$$\nabla \times \nabla \psi = 0 \tag{2.28}$$

and

$$\nabla \cdot \nabla \times F = 0 \tag{2.29}$$

for an arbitrary scalar field ψ and vector field F [34].

Gauss' law 2.23 along with Eq. 2.29 are satisfied if we define A such that

$$B = \nabla \times A. \tag{2.30}$$

The electric potential ϕ is then defined as

$$E = -\nabla \phi. \tag{2.31}$$

Substituting the above equation in Eq. 2.26 and using the Eq. 2.28 leads to

$$\nabla \times (-\nabla \phi) = 0.$$

Using Ohm's law, Eq. 2.27, and the definition of the electric potential function ϕ, Eq. 2.31, the following expression for the current density j is obtained

$$j = -\sigma_m \nabla \phi. \tag{2.32}$$

Combining the charge conservation Eq. 2.22 and the modified Ohm's law 2.32, the electric potential equation is written as

$$\nabla \cdot (\sigma_m \nabla \phi) = 0$$

where the magnetic conductivity σ_m is a function of temperature. It is given later on for an argon gas.

Combining the simplified Ampere's law, Eq. 2.25, and Eq. 2.30 yields

$$\nabla \times \nabla \times A = -\mu_0 \sigma_m \nabla \phi$$

Using the property of the operator $(\nabla \times \nabla \times)$ leads to

$$\nabla(\nabla \cdot A) - \nabla^2 A = -\sigma_m \mu_0 \nabla \phi. \tag{2.33}$$

The electric and magnetic fields are written in terms of scalar and vector potentials as in Eqs. 2.31 and 2.30. However many different potentials that can generate the same fields. According to the *Helmholtz* theorem of vector analysis, a vector is uniquely defined if and only if both its curl and divergence are specified [34]. In order to get a unique solution one may choose the divergence of A so that the differential Eq. 2.33 has the simplest possible form. This is achieved with the Coulomb gauge condition $(\nabla \cdot A = 0)$ that leads to a Poisson equation for the magnetic field

$$\nabla^2 A = \sigma_m \mu_0 \nabla \phi.$$

The Maxwell's equations, when expressed in terms of the potentials ϕ and A, are then reduced to the following form

$$\nabla \cdot (\sigma_m \nabla \phi) = 0, \tag{2.34}$$
$$\nabla^2 A = \sigma_m \mu_0 \nabla \phi. \tag{2.35}$$

In other words, the electric and magnetic potentials satisfying these equations always lead to a solution of Maxwell's equations for E and B when used with Eqs. 2.31 and 2.30.

2.1.6 Calculation of the magnetic field for 2D axi-symmetric problems

In the 2D and axi-symmetric case the calculation of the magnetic field can be simplified. Since the current density is axi-symmetric, the self induced θ component of the magnetic field B can be derived from Ampere's law:

$$\frac{\partial B_\theta}{\partial r} = -\mu_0 j_x$$

where a cylindrical coordinate system (r, θ, x) is used.

As a result, it is required to solve the electric potential equation

$$\nabla \cdot (\sigma_m \nabla \phi) = 0$$

in order to get the electric current density:

$$j = -\sigma_m \nabla \phi.$$

2.2 Thermodynamic and transport properties

The first role of the shielding gas is to protect the melted metal from oxidation by the surrounding air. The selection of shielding gas depends on several factors, among them on its ability to conduct heat, as the heat source must be suited to the type of material being welded and the joint design. Argon is the most commonly used shielding gas for GTAW.

In the welding process the temperature gradient is very large. As a result the thermodynamic and transport properties of the argon gas exhibit strong variations with temperature. A direct measurement of the thermodynamic properties is difficult at high temperatures on the other hand, kinetic theory is not always valid at low temperature when the gas density gets too large. Due to this fact, the data of the physical properties based on experimental measurements at low temperatures was combined with the data obtained from kinetic theory at high temperatures. Due to very high plasma temperatures, radiation is also an important phenomena which has to be accounted for.

This section describes the composition of a simple argon gas as a function of temperature, followed by a description of the physical properties of the gas for the considered temperature range. The thermodynamic properties and transport coefficients that are measured experimentally and derived with the kinetic theory are displayed. The radiation loss is also discussed.

2.2.1 Composition of a simple argon gas

In welding applications the heavy species (atoms and ions) do not have enough energy to promote or initiate ionization. The electrons, that have a smaller mass than the ions can be more easily accelerated and reach a kinetic energy larger than the ionization threshold. They can thus provide the energy for ionization.

When a monoatomic gas such as argon is progressively heated the atoms first ionize

$$Ar + e \rightleftarrows Ar^+ + e + e$$

where the e on the left side of this equation represents an electron that brings the energy necessary for ionization.

A further increase in temperature causes Ar^+ ions to lose one more electron, this is the second ionization step

$$Ar^+ + e \rightleftarrows Ar^{++} + e + e$$

At higher temperatures the third ionization step begins

$$Ar^{++} + e \rightleftarrows Ar^{+++} + e + e$$

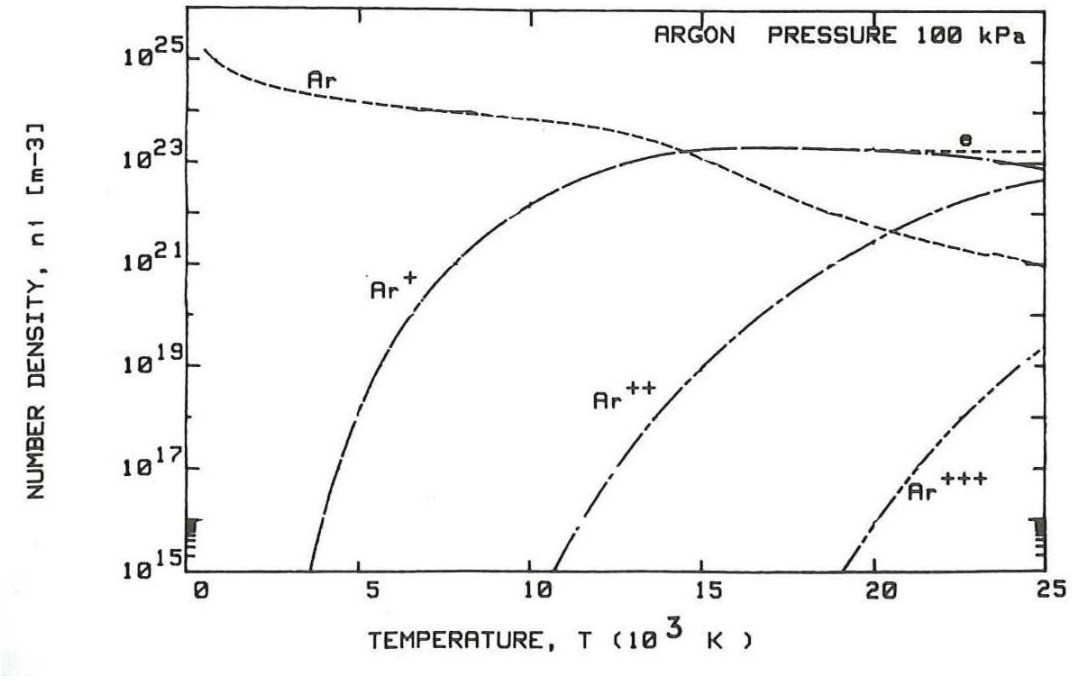

Figure 2.1: Temperature dependence of the equilibrium composition (species number densities) of an argon plasma at atmospheric pressure (starting from one mole of Ar at room temperature [21].)

.

Figure 2.1 shows the temperature dependence of the argon plasma at chemical equilibrium and at atmospheric pressure, starting from room temperature. As the temperature increases, the particle density decreases monotonically due to the progressive first ionization. From about 15000 K, the number density of Ar^+ decreases steadily while Ar^{++} is formed and the electron density is not significantly changed at the temperature range from 15000 K up to 25000 K. At 25000 K the number density of Ar^{+++} is still two orders of magnitude less than for Ar and four orders less than Ar^+ and Ar^{++}.

Figure 2.1 illustrates that the composition of the gas changes because of the ionization process. This change is included in the model used for the transport and thermophysical properties of the argon plasma.

2.2.2 Summary of the thermal plasma properties

In the present work the temperature can vary from 300 up to 30000 K. Experimental data collected in [31] for the low temperature range of [200, 1400] K were combined together with the data obtained from kinetic theory for the high temperature range [500, 30000] K [50]-[51]. It was checked that these data do overlap correctly in the common range of validity, see Appendix A.

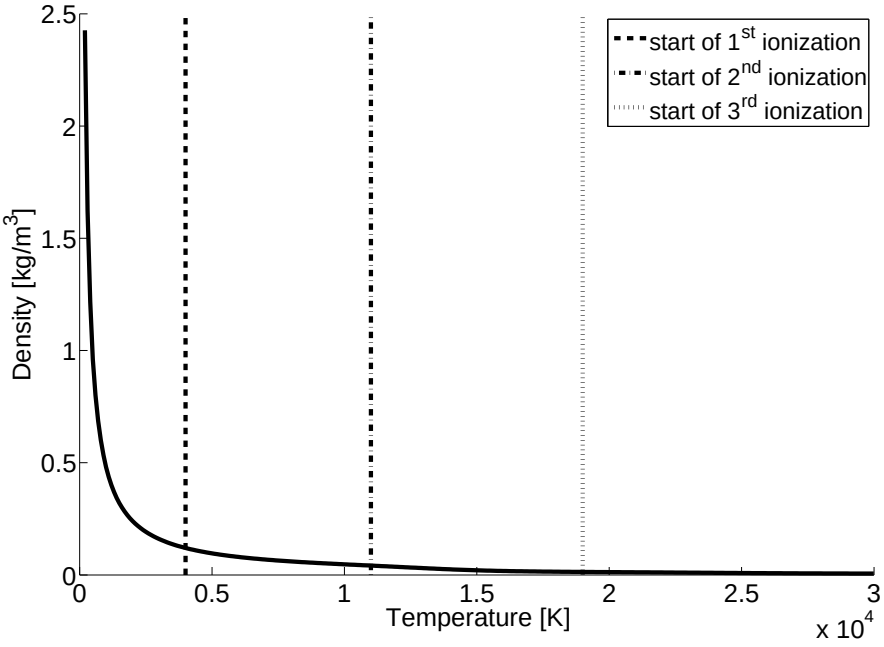

Figure 2.2: Density of an argon gas versus temperature .

The resulting density profile that was used in the simulations done in the present work is shown in Figure 2.2. As it can be seen, the density is constantly decreasing with the increasing temperature. Even before the first ionization, the density has already significantly reduced.

Similar assembling of experimental data in the low temperature range of [200, 1400] K and kinetic theory values in the range of [500, 30000] K have been done for the rest of the thermodynamic and transport properties. The resulting viscosity, thermal conductivity, heat capacity at constant pressure and enthalpy are plotted as function of the temperature in Figures 2.3-2.6, respectively

Finally, the net emission coefficient, ϵ_N, that is used to represent the

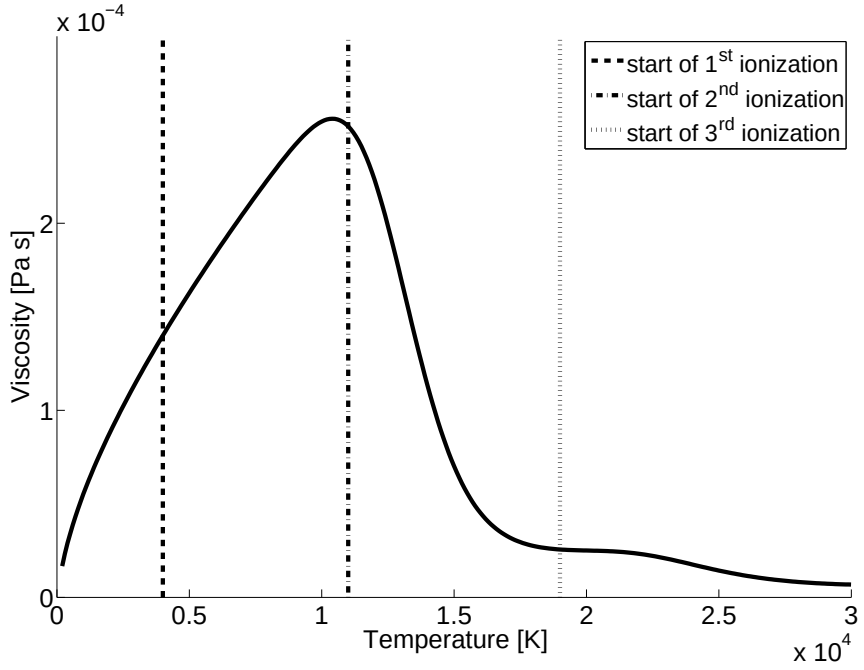

Figure 2.3: Viscosity of an argon gas versus temperature.

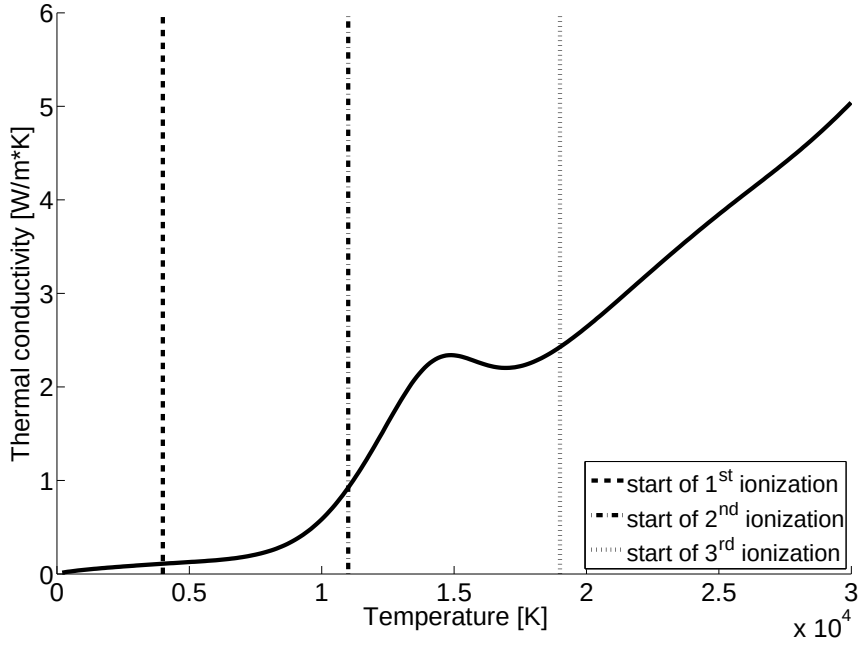

Figure 2.4: Thermal conductivity of an argon gas versus temperature.

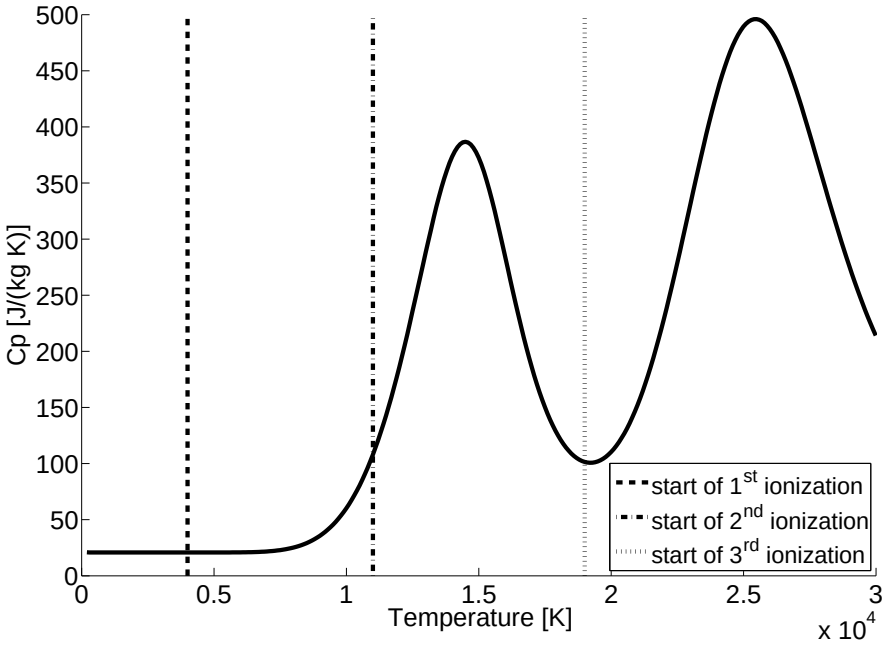

Figure 2.5: Heat capacity at constant pressure of an argon gas versus temperature.

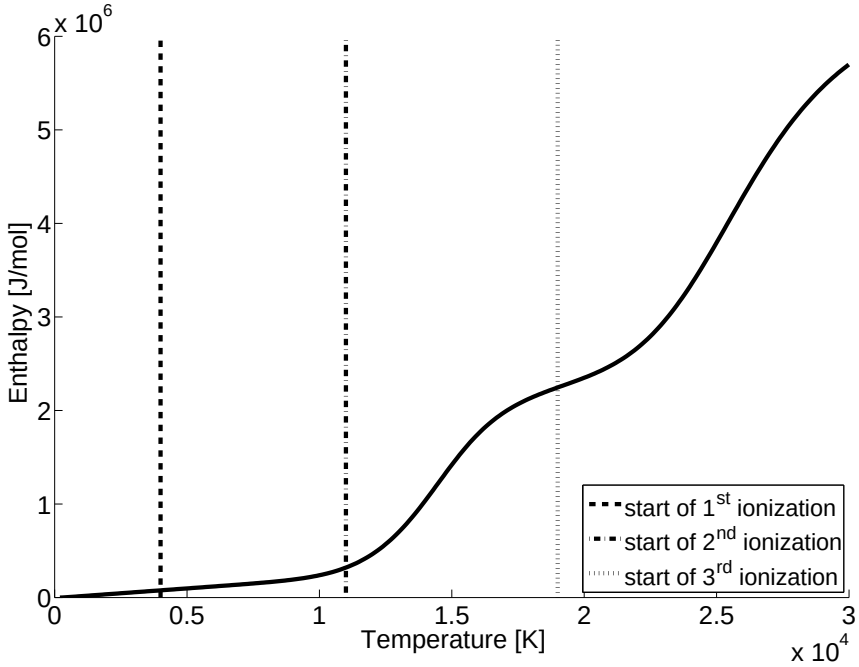

Figure 2.6: Enthalpy of an argon gas versus temperature.

radiative cooling, see Eq. 2.3, is presented in Fig. 2.7. As shown, a sharp increase is observed after the beginning of the second and third ionizations.

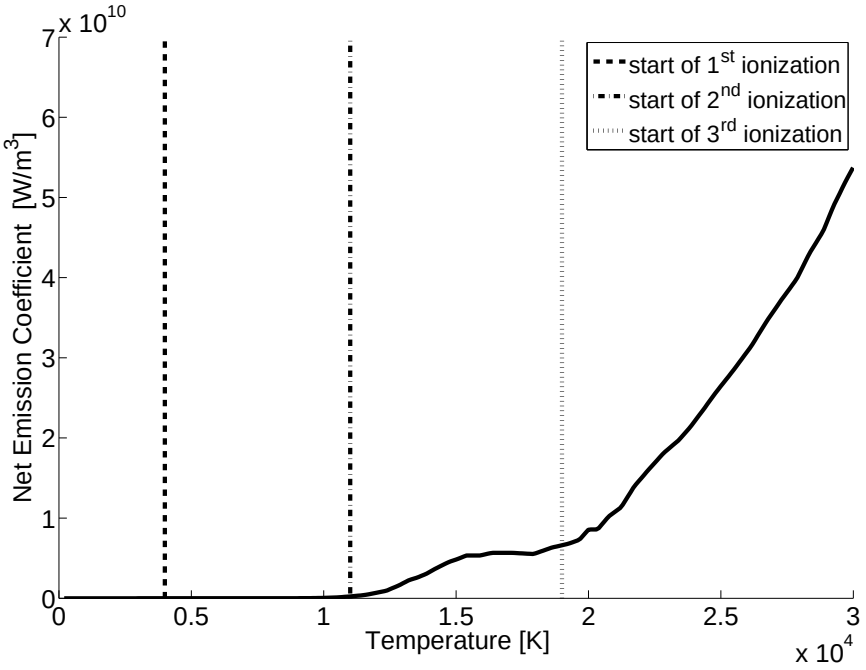

Figure 2.7: Net emission coefficient of an argon gas.

2.3 Summary of arc column modeling

In this section, a summary of the mathematical model for a transferred arc is presented.

Assumptions:

- The plasma is a Newtonian fluid.
- The plasma column is supposed to be in local thermodynamic equilibrium (LTE). This implies that the temperatures of the electrons and the heavy particle are the same. This assumption is valid in the arc column region, but will break down near the electrodes [21].
- The flow of the heat conducting viscous fluid is laminar and mechanically incompressible, but thermally expansible .
- The arc column plasma is electrically neutral.
- The electromagnetic phenomena is steady.
- The induction and Hall currents are negligible.
- The plasma is optically thin, i.e no absorbation is taking place inside the arc.

Governing equations:

- Conservation of mass:

$$\frac{\partial}{\partial t}\rho + \nabla \cdot (\rho U) = 0 \tag{2.36}$$

- Conservation of momentum:

$$\begin{aligned}\frac{\partial}{\partial t}(\rho U) + \nabla \cdot (\rho U U) - \nabla \cdot [\mu(\nabla U + (\nabla U)^T) \\ -\frac{2}{3}\mu(\nabla \cdot U)I] = -\nabla p + \underbrace{j \times B}_{\text{Lorenz force}}\end{aligned} \tag{2.37}$$

- Enthalpy conservation equation:

$$\begin{aligned}\frac{\partial}{\partial t}(\rho h) + \nabla \cdot (\rho U h) - h\nabla \cdot \rho U - \nabla \cdot (\alpha \nabla h) = \nabla \cdot (Up) \\ -p\nabla \cdot U + \underbrace{j \cdot E}_{\text{Joule heating}} - S_r + S_e\end{aligned} \tag{2.38}$$

- Maxwell's equations in potential formulation:

$$\nabla \cdot (\sigma_m \nabla \phi) = 0 \tag{2.39}$$

$$\nabla^2 A = \sigma_m \mu_0 \nabla \phi \tag{2.40}$$

The coupling between the magnetic problem and the momentum and enthalpy equation is established through the Joule heat source, the Lorentz force, and through the temperature dependance of the electrical conductivity.

A discussions of the algorithm and tools that were used to solve this problem will be presented in Chapter 3. The numerical details are given in Appendix B.

Chapter 3

Implementation and validation

The system of equations 2.36-2.40 that have been introduced in Chapter 2 and supplemented with the constitutive relations, initial and boundary conditions has generally no analytical solution. Therefore a numerical solution is usually sought.

In the frame of this work, a numerical tool was developed that is based on OpenFOAM (*www.openfoam.org*), a general purpose open-source CFD code. This code is based on the finite volume method and has a capacity to perform three-dimensional unsteady simulations. In this chapter details on the development of the simulation tool are presented. First, the capability of the relevant already existing solver is described. This is followed by the extensions that have been implemented in order to fit the solver in the frame of arc welding. Finally, a validation of the complete model, as well as its separate electromagnetic part, is presented. For the convenience of the reader, the details of the numerical modelling are separately described in Appendix B.

3.1 Development in OpenFOAM

The development of the solver for the arc welding simulations is based on the existing *buoyantSimpleFoam* solver, which is a standard steady-state OpenFOAM solver for buoyant, turbulent flow of compressible fluids for ventilation and heat-transfer.

The following equations are solved in the *buoyantSimpleFoam* solver:

- Conservation of mass

$$\nabla \cdot (\rho U) = 0$$

  where U is the velocity of the flow and ρ is the density that can be constant or modeled by an ideal gas law .

- Conservation of momentum

$$\nabla \cdot (\rho UU) - \nabla \cdot [\mu_{eff}(\nabla U + (\nabla U)^T) - \frac{2}{3}\mu_{eff}(\nabla \cdot U)I] = -\nabla p$$

where $p = p_s + \rho \cdot g_h + p_{ref}$ and p_s is the static pressure, p_{ref} is the reference pressure and $\rho \cdot g_h$ is the body force due to the gravitation. Here I the the unit tensor and μ_{eff} the effective viscosity. The effective viscosity is represented by

$$\mu_{eff} = \mu_{lam} + \mu_{turb}$$

with μ_{lam} and μ_{turb} being the laminar and the turbulent kinetic viscosities, respectively. The laminar kinetic viscosity μ_{lam} is given either as a constant value or defined using a Janaf table.

- Conservation of enthalpy

$$\nabla \cdot (\rho Uh) - h\nabla \cdot \rho U - \nabla \cdot (\alpha_{eff}\nabla h) = \nabla \cdot (Up) - p\nabla \cdot U$$

where h is the enthalpy and α_{eff} denotes the effective thermal diffusivity, represented by

$$\alpha_{eff} = \alpha_{lam} + \alpha_{turb}.$$

Here α_{lam} and α_{turb} denotes the laminar and the turbulent thermal diffusivities, respectively. Similar to the viscosity, α_{lam} is either a constant or attains its value from a Janaf table.

The temperature is defined from the specific enthalpy using the definition of the specific heat capacity at constant pressure

$$c_p = \left(\frac{\partial h}{\partial T}\right)_p$$

where c_p is either a constant or modeled using a Janaf table.

Comparing this system of equations with the system that was presented in Chapter 2, the following differences can be observed:

- The transport and thermodynamic properties of the fluid that are available in the *buoyantSimpleFoam* solver can be a constant or modeled via a Janaf table. The upper limit for the temperature is thus approximately 5000 K. In this work the properties of the fluid strongly

depend on the temperature that is varying from 300 up to 30000 K. Therefore, the modeling of transport and thermodynamic properties in the *buoyantSimpleFoam* solver has been modified in accordance with the discussions in Chapter 2. Moreover, since the flow is considered to be laminar only the laminar part of the effective viscosity and thermal diffusivity is remained.

- Due to the fact that the temperature gradient is very large in the domain and the flow is thermally expansible, the density should not be a constant or modeled by the ideal gas law as it is done in the *buoyantSimpleFoam* solver. As a result, the modeling of the density in the *buoyantSimpleFoam* solver have been modified in accordance with the discussions in Chapter 2.

- In the absence of buoyancy effects the body force due to the gravitation is neglected.

- The electromagnetic equations, as well as the transport of the electron enthalpy and radiative loss per unit volume source terms are not modeled in the *buoyantSimpleFoam* solver. Therefore relevant electromagnetic equations and source terms that are missing in the momentum and the energy equations have been implemented.

In order to develop the solver for arc welding problems, the *buoyantSimpleFoam* solver is completed with the set of equations that represent the electromagnetic part. In addition, the necessary source terms in the momentum and enthalpy equations to account for the Lorenz force, Joule heating, radiative cooling and transport of the electron enthalpy have been included. The model is not designed to handle the arc ignition. In the beginning of the simulation there is no plasma in the computational domain and a large potential difference is imposed. As a result, the Joule source term in the enthalpy equation is becoming very large and the calculation diverges. In order to solve this problem a weight function technique proposed by Baudry [28] is used. The summarized system of equations that was implemented is listed below:

- Conservation of mass:

$$\frac{\partial}{\partial t}\rho + \nabla \cdot (\rho U) = 0$$

- Conservation of momentum:

$$\frac{\partial}{\partial t}(\rho U) + \nabla \cdot (\rho U U) - U\nabla \cdot \rho U + \nabla \cdot [\mu_{lam}(\nabla U + (\nabla U)^T) - \frac{2}{3}\mu_{lam}(\nabla \cdot U)I] = -\nabla p + \underbrace{j \times B}_{\text{Lorenz force}}$$

- Enthalpy equation:

$$\frac{\partial}{\partial t}(\rho h) + \nabla \cdot (\rho U h) - h\nabla \cdot \rho U - \nabla \cdot (\alpha_{lam} \nabla h) = \nabla \cdot (Up)$$
$$-p\nabla \cdot U + \underbrace{\omega \cdot (j \cdot E)}_{\text{Joule heating}} - \underbrace{4\pi\epsilon_N}_{\text{Radiation loss}} + \underbrace{\nabla \cdot \left(\frac{5k_b j}{2ec_p} h\right)}_{\text{Transport of the electron enthalpy}}$$

- Maxwell's equations in potential formulation:

$$\nabla \cdot (\sigma_m \nabla \phi) = 0$$
$$\nabla^2 A = \sigma_m \mu_0 \nabla \phi$$

The Joule heating term is expressed as

$$\omega \cdot (j \cdot E) = \omega \cdot (\sigma_m (\nabla \phi) \cdot (\nabla \phi))$$

where ω is the weight function that is used to control the Joule heating term and is calculated as

$$\omega = \sqrt{\frac{1}{f_{max}}}.$$

Here f_{max} denotes the maximum value of the vector function $\sigma(\nabla\phi)^2/(\rho h)$ at a given time step. After a few time steps, this weight function approaches unity and retains this value for the rest of computation. The complete solution sequence and its description is given in Appendix B.

3.2 Validation of the electromagnetic part

In this section the electromagnetic part of the solver is validated. The validation is performed for a case with a known analytic solution. In addition, various boundary conditions for the magnetic potential vector have also been evaluated.

3.2.1 Infinite electric rod

Consider an infinite rod of constant radius r_0, with a constant current density parallel to the rod axis, see Figure 3.1. The electrical conductivity is defined as a constant inside the rod, representing a hot argon gas column at a fixed temperature of $T = 10600$ K.

It is known that the analytic solution is reduced to an x component of the magnetic potential vector A and a θ component for the magnetic field B. The other components of these vectors are equal to zero. Inside the

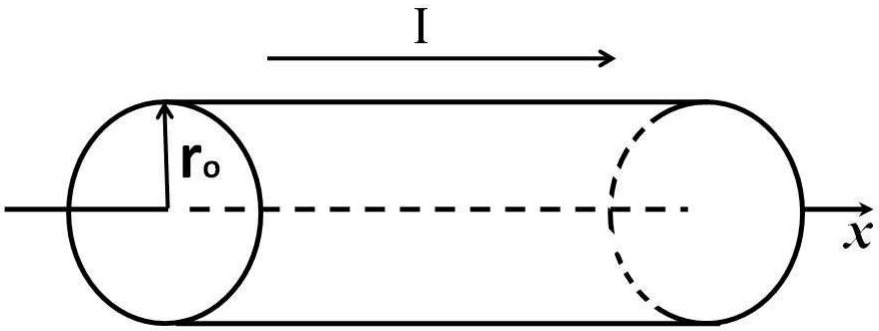

Figure 3.1: Electric rod.

cylinder, the analytic solution of the magnetic potential vector is expressed as follows

$$A_{x,in} = A_0 - \frac{\mu_0 J_x r^2}{4} \quad \text{if } r \leq r_0. \tag{3.1}$$

Outside the cylinder it is given by the following expression

$$A_{x,out} = A_0 - \frac{\mu_0 J_x r^2}{2}[0.5 + ln(r/r_0)] \quad \text{if } r > r_0 \tag{3.2}$$

where μ_0 is the magnetic permeability of vacuum and J_x is the current density. In this test case J_x can be found via the current intensity I from the following expression

$$J_x = \frac{I}{\pi r_0^2}.$$

In both Eqs. 3.1 and 3.2, A_0 denotes the reference value that was chosen in such a way so that the numerical and analytical solutions are comparable.

The magnetic field and the magnetic potential vector are linked by the relation $\vec{B} = \nabla \times \vec{A}$. Integrating Eqs. 3.1 and 3.2 the following analytic expressions are obtained for the magnetic field inside the cylinder

$$B_{\theta,in} = \frac{\mu_0 J_x r}{2} \quad \text{if } r \leq r_0, \tag{3.3}$$

and outside the cylinder

$$B_{\theta,out} = \frac{\mu_0 J_x r_0^2}{2r} \quad \text{if } r > r_0. \tag{3.4}$$

3.2.2 Description of the simulations

The analytical solution has been compared with the numerical results obtained with the help of the developed solver. The configuration of the rod is summarized in Table 3.1.

I[A]	r_0 [m]	r_t [m]	σ_{in} $[A/(V \cdot m)]$	σ_{out} $[A/(V \cdot m)]$	L [m]
600	10^{-3}	0.1	2700	10^{-5}	10^{-2}

Table 3.1: Rod case parameters.

.

Here I is the current intensity, r_0 the radius of the rod, r_t the total radius of the domain and L denotes the length of the rod. The electrical conductivities inside and outside of the rod are denoted by σ_{in} and σ_{out}, respectively. In addition, σ_{in} corresponds to the electrical conductivity of argon gas at 10600 K.

The simulation is run as 2D and axi-symmetric. OpenFOAM needs 3D control volumes even for 2D cases, with one control volume in the third direction. The solution procedure is reduced to 2D by choosing a specific boundary condition in the third direction. For 2D axi-symmetric problems this boundary condition is named *wedge*. The geometry should form a wedge of 5° angle, with symmetry axis along the x axis and center plane at $z = 0$. Figure 3.2 shows a sketch of the computational domain. Here, *"block 0"* corresponds to the rod and *"block 1"* represents the atmosphere. A uniform mesh was used in the present simulation.

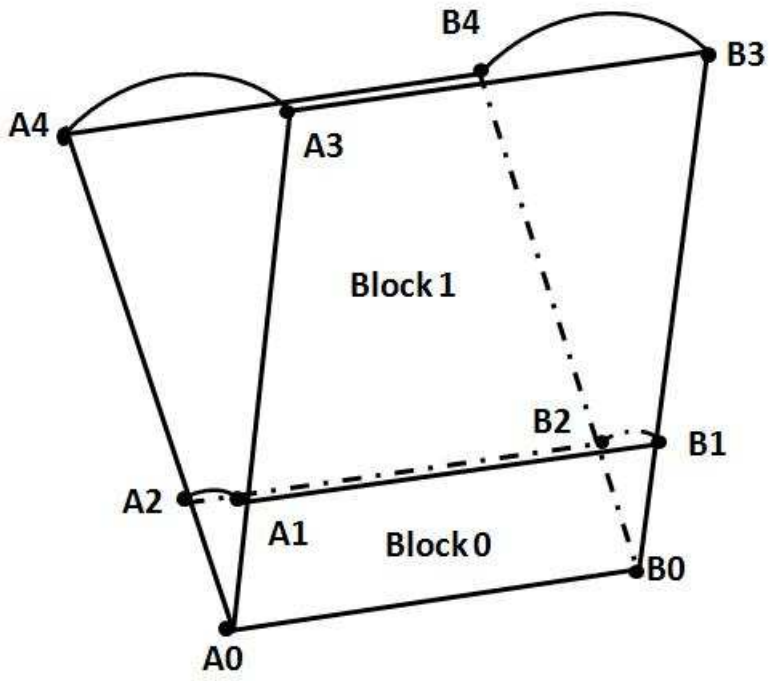

Figure 3.2: Computational domain.

The boundary conditions used for the magnetic potential vector A and the electric potential ϕ are summarized in Table 3.2, where n denotes the outward normal vector to a surface.

$A_0A_1A_2$	$B_0B_1B_2$	$A_2A_1A_4A_3$	$B_2B_1B_4B_3$	$A_4A_3B_3B_4$
$\frac{\partial A}{\partial n} = 0$	$\frac{\partial A}{\partial n} = 0$	$\frac{\partial A}{\partial n} = 0$	$\frac{\partial A}{\partial n} = 0$	$A = 0$
$\phi = 707$	$\phi = 0$	$\frac{\partial \phi}{\partial n} = 0$	$\frac{\partial \phi}{\partial n} = 0$	$\frac{\partial \phi}{\partial n} = 0$

Table 3.2: Boundary conditions.

3.2.3 Results and validation

The numerical result obtained for this simulation is presented in Figure 3.3. As expected, the current density is going from left to right (from high to low electric potential) and is perpendicular to the iso-lines of electric potential inside the rod. The iso-lines of the electric potential are parallel to each other inside the rod and curving out outside the rod. This behaviour is mainly due to the used boundary conditions. Since the electric conductivity of the outer region is very small, $\sigma_{out} = 10^{-5}$, the current leakage is negligible.

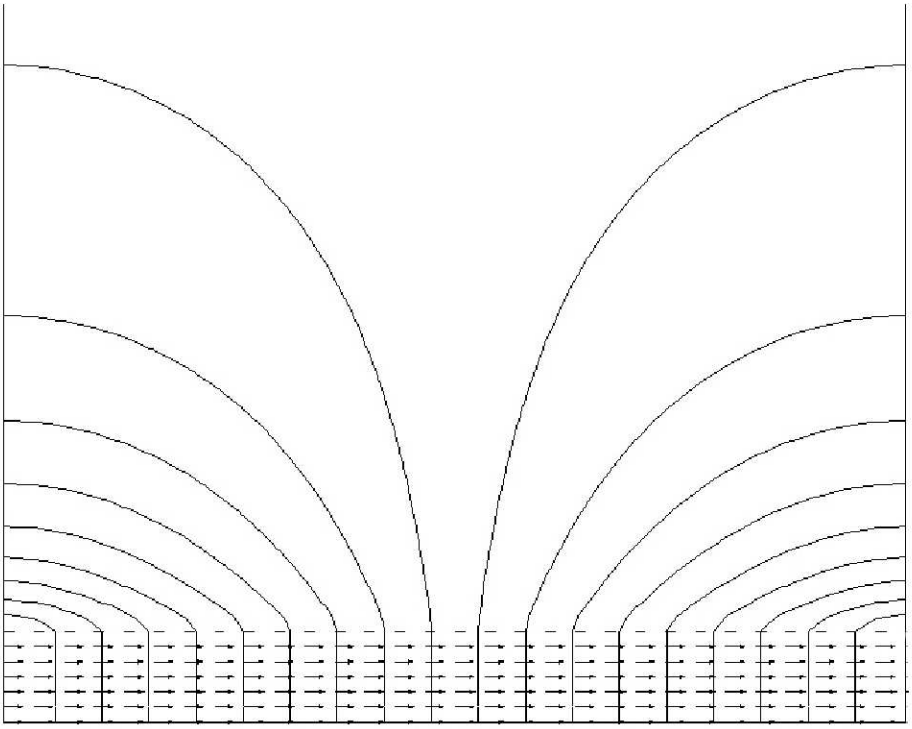

Figure 3.3: The electric potential iso-lines together with current density vectors. Zoom near the rod.

Figures 3.4 and 3.5 show a comparison of the numerical and the analytic solutions.

As it can be seen from Fig. 3.4, the profiles of the computed magnetic potential vector A are in good agreement with the analytical values. Close to the interface between the rod and the atmosphere, and at the symmetry

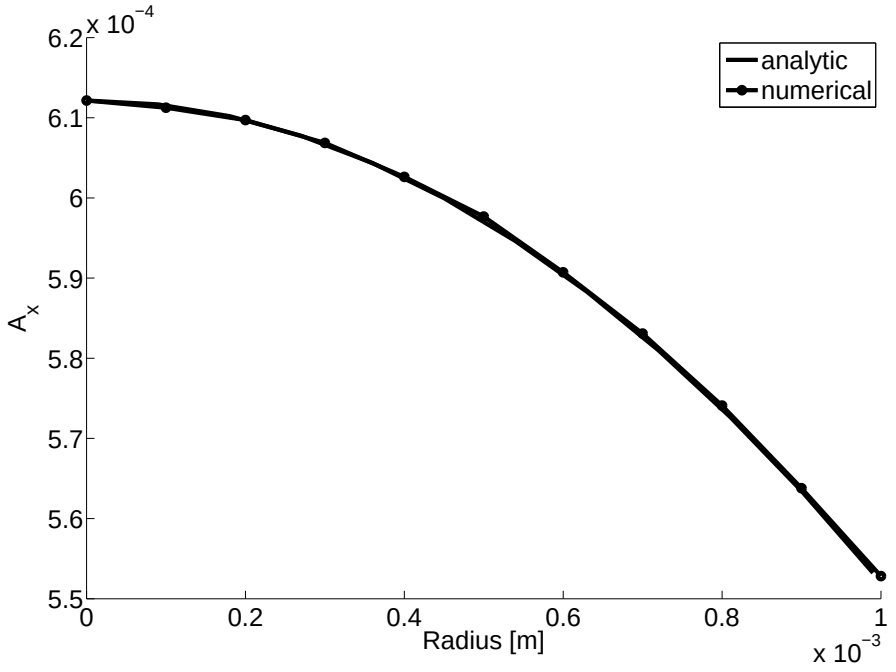

(a) Zoom at the rod region.

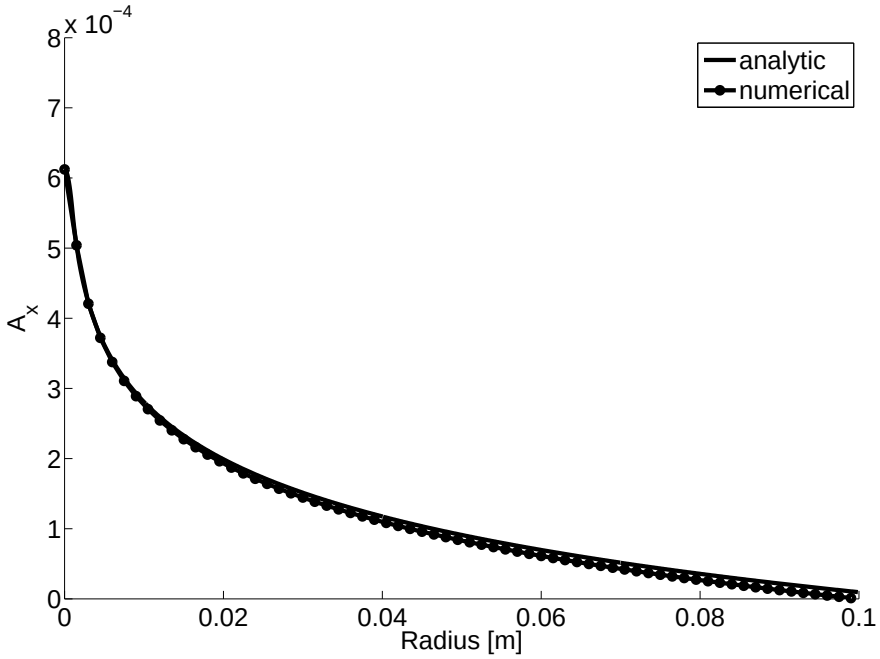

(b) The complete length of the domain.

Figure 3.4: x-component of the magnetic potential vector A along the radius of the domain (at $x = 0.5 \cdot 10^{-2}$ [m]).

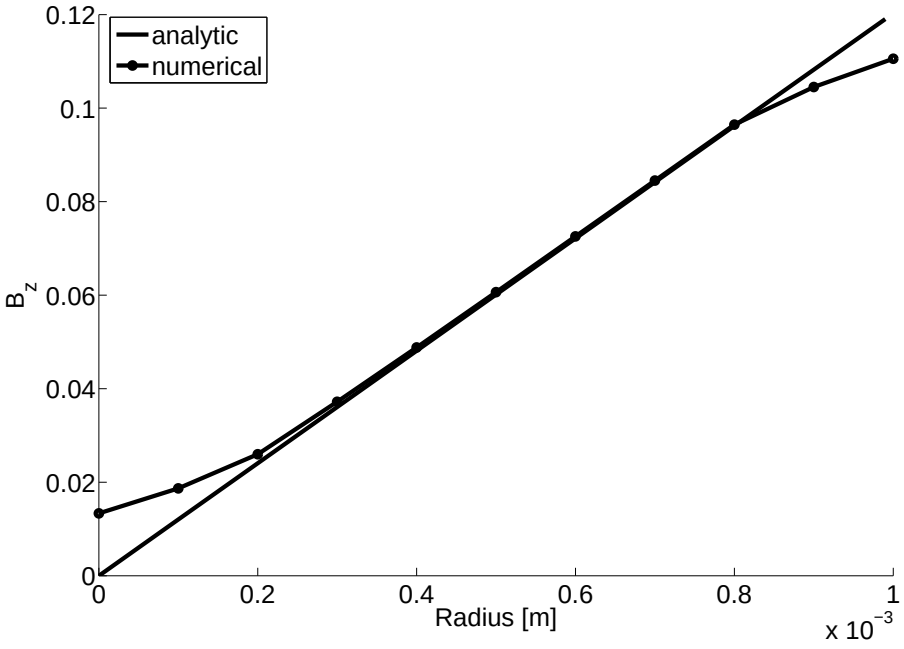

(a) Zoom at rod region.

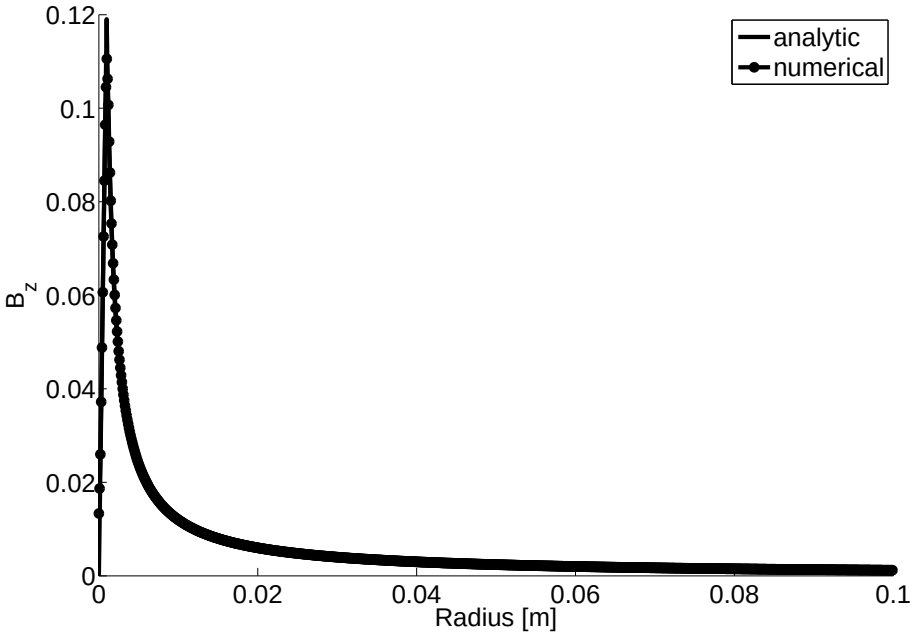

(b) The complete length of the domain.

Figure 3.5: z-component of the magnetic field B along the radius of the domain (at $x = 0.5 \cdot 10^{-2}$ [m]).

axis, a small difference in the magnetic field B is observed, see Fig. 3.5. This is, most likely, due to the fact that the mesh is not sufficiently refined in these regions and that no special treatment of the sharp gradient of σ has been implemented.

3.2.4 Test of boundary conditions

As it was previously mentioned, the rod case was also used to investigate appropriate boundary conditions for the magnetic potential vector, in view of the transferred arc case of Tsai and Sindo [24].

In this case the computational domain was resized in order to have it more similar to the computational domain of the *transferred arc* case. The total radius of the computational domain, $B_0B_3 = 16$ mm, corresponds to the anode radius and the radius of the rod, $B_0B_1 = 0.5$ mm, corresponds to the radius of the electrode tip of the *transferred arc* test case, see Fig. 3.6. Here two reference points are represented by R_{side} and R_{top}.

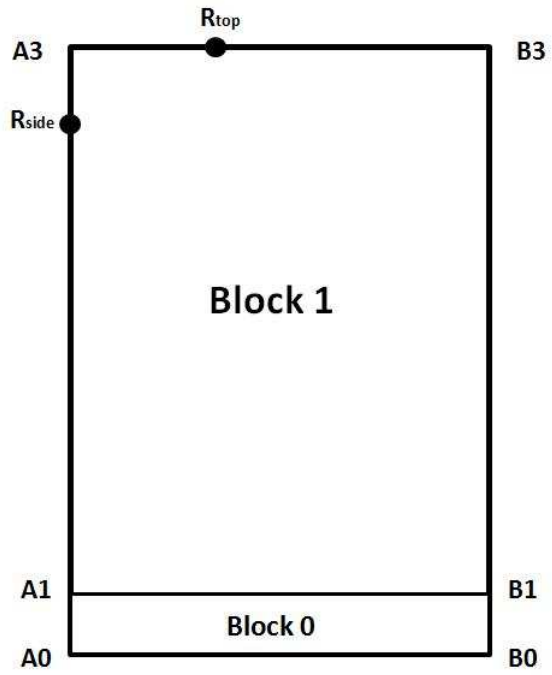

Figure 3.6: Resized computational domain.

The following cases have been studied:

- 1^{st} *test case:* This case uses the boundary conditions in Table 3.3.
- 2^{nd} *test case:* This case uses the boundary conditions in Table 3.4 and also set $A = 0$ at R_{top}.
- 3^{rd} *test case:* This case uses the boundary conditions in Table 3.4 and also sets $A = 0$ at R_{side}.

A_0A_1	A_1A_3	B_0B_1	B_1B_3	A_3B_3
$\frac{\partial A}{\partial n} = 0$	$\frac{\partial A}{\partial n} = 0$	$\frac{\partial A}{\partial n} = 0$	$\frac{\partial A}{\partial n} = 0$	$A = 0$
$\phi = 707$	$\frac{\partial \phi}{\partial n} = 0$	$\phi = 0$	$\frac{\partial \phi}{\partial n} = 0$	$\frac{\partial \phi}{\partial n} = 0$

Table 3.3: Boundary conditions, 1^{st} test case.

A_0A_1	A_1A_3	B_0B_1	B_1B_3	A_3B_3
$\frac{\partial A}{\partial n} = 0$	$\frac{\partial A}{\partial n} = 0$	$\frac{\partial A}{\partial n} = 0$	$\frac{\partial A}{\partial n} = 0$	$\frac{\partial A}{\partial n} = 0$
$\phi = 707$	$\frac{\partial \phi}{\partial n} = 0$	$\phi = 0$	$\frac{\partial \phi}{\partial n} = 0$	$\frac{\partial \phi}{\partial n} = 0$

Table 3.4: Boundary conditions, 2^{nd} and 3^{rd} test case.

- 4^{th} *test case:* This case uses the boundary conditions in Table 3.5.

A_0A_1	A_1A_3	B_0B_1	B_1B_3	A_3B_3
$\frac{\partial A}{\partial n} = 0$	$A = 0$	$\frac{\partial A}{\partial n} = 0$	$\frac{\partial A}{\partial n} = 0$	$\frac{\partial A}{\partial n} = 0$
$\phi = 707$	$\frac{\partial \phi}{\partial n} = 0$	$\phi = 0$	$\frac{\partial \phi}{\partial n} = 0$	$\frac{\partial \phi}{\partial n} = 0$

Table 3.5: Boundary conditions, 4^{th} test case.

A comparison of the numerical results for these cases and the analytic solution is presented in Figures 3.7 and 3.8.

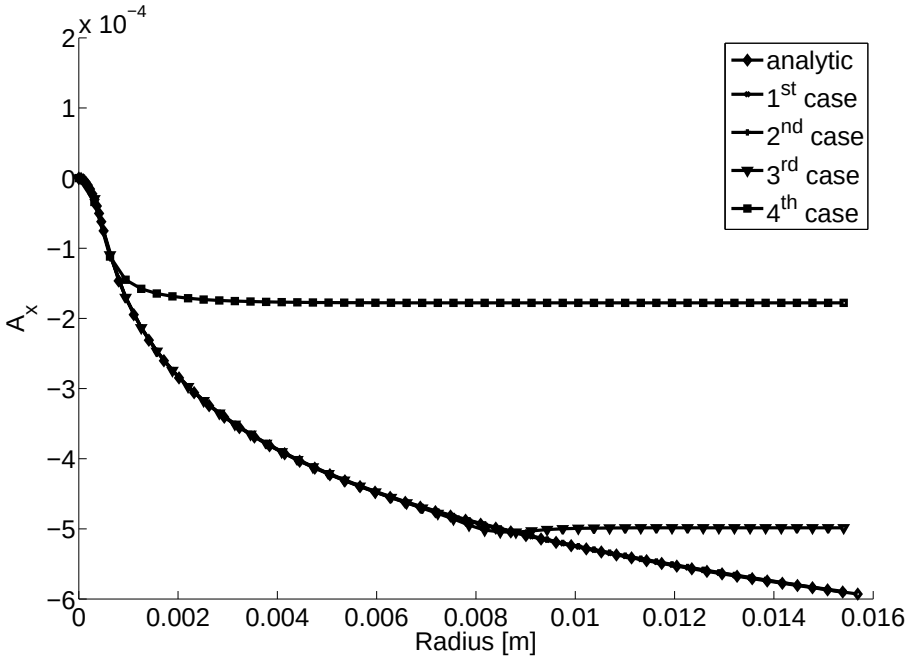

Figure 3.7: x-component of magnetic potential vector A along the radius of the domain.

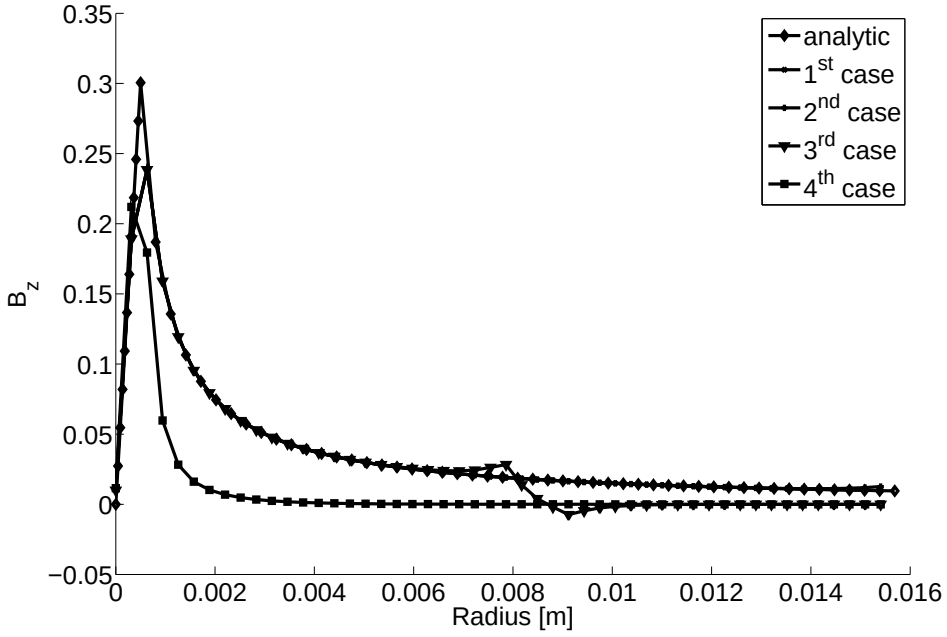

Figure 3.8: z-component of the magnetic field B along the radius of the domain.

As it can be seen, the best agreement is obtained for 1^{st} and 2^{nd} cases. As a result, for the case that represents a transferred arc configuration,

the Dirichlet boundary condition for the magnetic potential vector on the outlet region of the domain will be used, as in the 1^{st} case.

3.3 Transferred arc configuration – 2D axi-symmetric test case

In this section the 2D transferred arc case is described and the numerical solution is presented.

3.3.1 Problem description

Many of the published studies of arc plasma welding consider significantly long arcs. For example, in studies of Hsu [11] and McKelliget [9], a 10 *mm* long arc is studied. In the present case, the same geometry was used as in Tsai [24], where an arc length of 2 *mm* is modeled. This choice is indeed closer to the TIG applications used nowadays. A schematic representation of arc welding is shown in Figure 3.9.

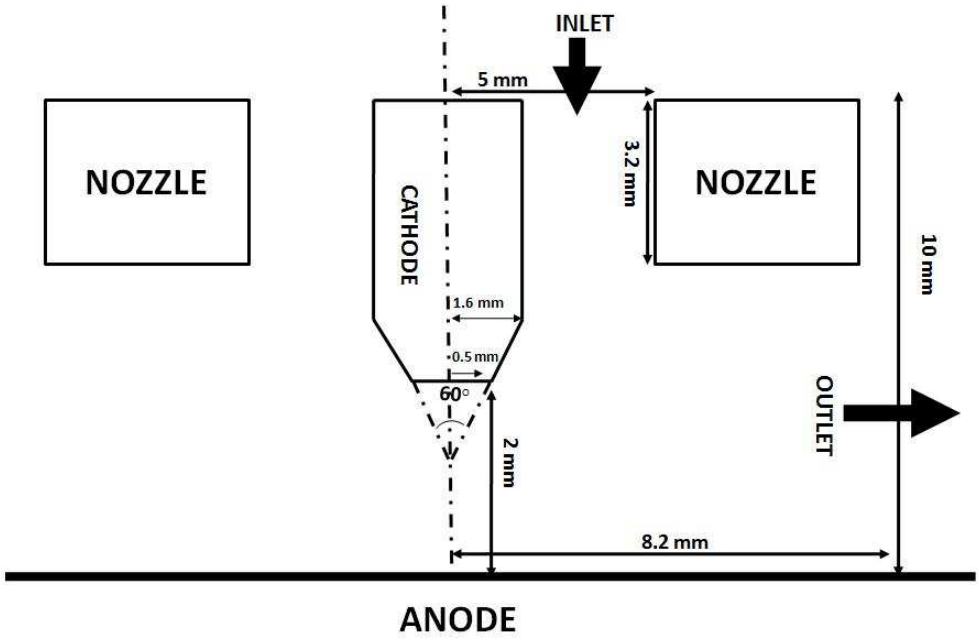

Figure 3.9: A schematic representation of 2D axi-symmetric arc welding.

The argon shielding gas is injected between a tungsten cathode and a ceramic nozzle. During the operation mode, an electric current that is a result of the applied voltage is going through the ionized argon gas between the tungsten cathode and the anode. The arc column is therefore formed between the cathode tip and the anode. For simulation of this case the following simplifying assumptions were made:

- The anode surface is considered to be flat.
- The problem is axi-symmetric.
- Gravity and heat dissipation due to viscous effects are negligible, due to high current [30].

These assumptions are supplemented with those presented in Chapter 2. The mathematical model is based on Eqs. 2.36- 2.39, written in Cartesian coordinates. Two different ways of calculating the magnetic field B are studied.

3.3.2 Description of the cases

The computational domain is restricted to a sector with one control volume in the tangential direction according to the methodology for performing axi-symmetric simulations in OpenFOAM, see Fig 3.10. The dimensions of the geometry are given in Fig 3.9.

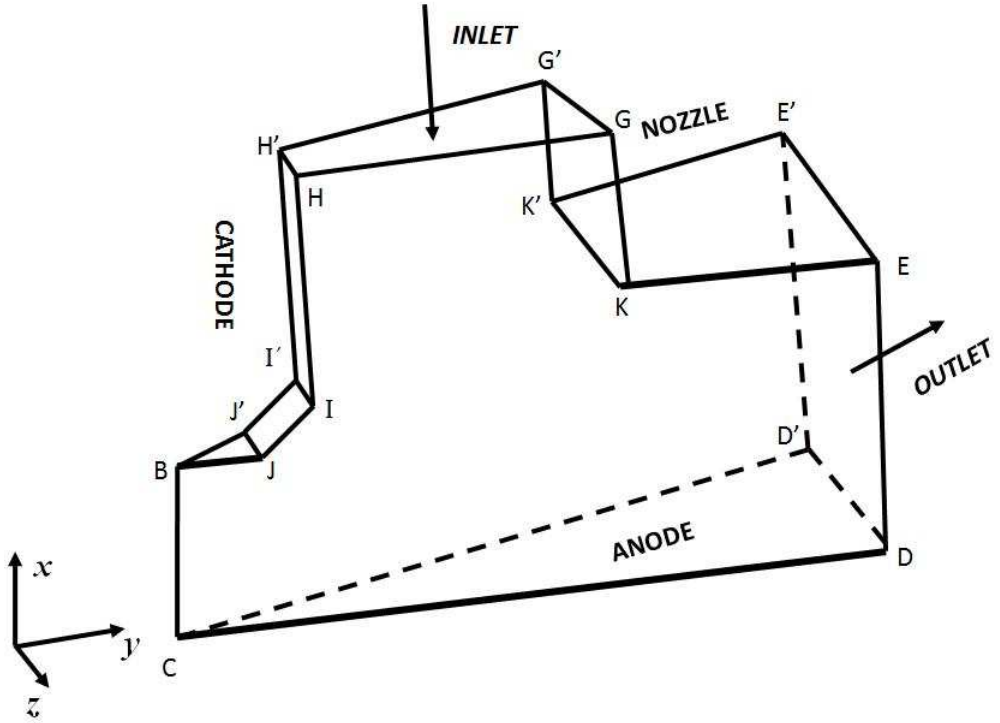

Figure 3.10: The computational domain of the 2D axi-symmetric transferred arc test case.

With a flow rate of pure argon of $1.66 \cdot 10^{-4}\ m^3/s$ [29], the average inlet velocity is obtained

$$\bar{U} = \frac{Q}{A} = 2.36 \text{ m/s}$$

where Q is the volumetric flow rate and A is the area.

The inlet velocity was imposed as a parabolic velocity profile due to the viscous friction that makes the velocity of the inlet jet slow down to zero at the contact with the cathode and nozzle wall (no slip condition). The radial velocity distribution at the inlet is given by

$$U = U_{max}\frac{(r_{int} - r)(r - r_{ext})}{r_0^2} \tag{3.5}$$

where U_{max} is calculated using definition of the average velocity and the given volume flow rate, and

$$r_0 = 0.5 \cdot (r_{ext} - r_{int}).$$

Here $r_{ext} = 5$ [mm] and $r_{int} = 1.6$ [mm] denote the external and internal radiuses, respectively.

The current density distribution at the cathode is set to

$$\begin{aligned} j &= 0 && \text{along IHI'H',} \\ j &= j_t && \text{along BJB'J',} \\ j &= j_t(1 - l/L) && \text{along JIJ'I'} \end{aligned}$$

where l is the distance from point J along JI, $j_t = 0.7 \times 10^8$ $[Am^{-2}]$ and $L = 1.0$ $[mm]$ according to the work of Tsai and Kou [24]. Due to the fact that the problem is 2D and axi-symmetric, the magnetic field can be computed in two different ways, forming the two test cases.

Boundary	U	T	ϕ	p
CDD'	0	$T^{\star}_{exp}$	$\phi = 0$	$\frac{\partial p}{\partial n} = 0$
EDE'D'	$\frac{\partial U}{\partial n} = 0$	$\frac{\partial T}{\partial n} = 0$	$\frac{\partial \phi}{\partial n} = 0$	101334 Pa
KEK'E'	0	$\frac{\partial T}{\partial n} = 0$	$\frac{\partial \phi}{\partial n} = 0$	$\frac{\partial p}{\partial n} = 0$
GKG'K'	0	$\frac{\partial T}{\partial n} = 0$	$\frac{\partial \phi}{\partial n} = 0$	$\frac{\partial p}{\partial n} = 0$
HGH'G'	Eq. 3.5	$\frac{\partial T}{\partial n} = 0$	$\frac{\partial \phi}{\partial n} = 0$	$\frac{\partial p}{\partial n} = 0$
HIH'I'	0	T_{exp}	$\frac{\partial \phi}{\partial n} = 0$	$\frac{\partial p}{\partial n} = 0$
IJI'J'	0	T_{exp}	$\frac{\partial \phi}{\partial n} = \frac{-j}{\sigma_m(T)}$	$\frac{\partial p}{\partial n} = 0$
BJJ'	0	$T = 20000$ K	$\frac{\partial \phi}{\partial n} = \frac{-j}{\sigma_m(T)}$	$\frac{\partial p}{\partial n} = 0$

Table 3.6: Boundary conditions for the first and second cases.

.

The electrode surface temperature T_{exp} decreases linearly from 3200 [K] along the edge JJ' to 2700 [K] at edge HH' [24]. The thermal boundary condition along the anode surface was estimated from the work of Haddad and Farmer [29], see Figure 3.11. The contour values were first

linearly extrapolated onto the surface of the anode and these extrapolated values were used to define a piecewise linear polynom, $T^{\star}_{exp}$. This is a valid approximation since according to Tsai [24] the calculated temperature distribution in the arc plasma is not very sensitive to the temperature boundary conditions on the anode surface.

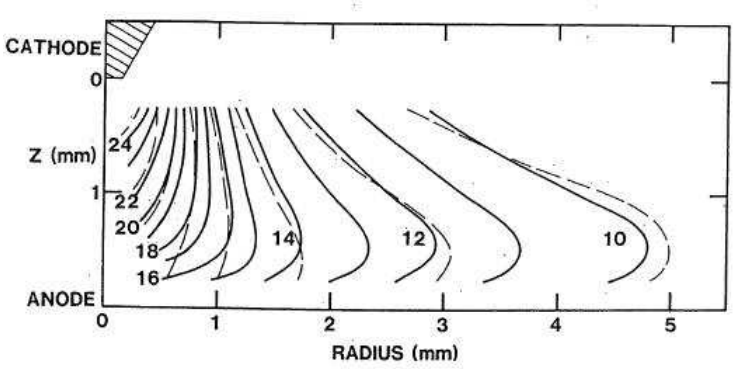

Figure 3.11: Measured temperature profile for a current intensity 200 A and 2 mm long arc [29].

- 1^{st} **test case:**

  The magnetic field is calculated as shown in Chapter 2 for the general 3D case, i.e. $B = \nabla \times A$. Therefore it is required to solve an extra equation

  $$\nabla^2 A = \sigma_m \mu_0 \nabla \phi.$$

  The boundary conditions are given in Tables 3.6 and 3.7.

CD	ED	KE	GK	HG	HI	IJ	BJ
$\frac{\partial A}{\partial n} = 0$	$A = 0$	$\frac{\partial A}{\partial n} = 0$	$\frac{\partial A}{\partial n} = 0$	$\frac{\partial A}{\partial n} = 0$	$\frac{\partial A}{\partial n} = 0$	$\frac{\partial A}{\partial n} = 0$	$\frac{\partial A}{\partial n} = 0$

Table 3.7: Boundary conditions of the magnetic potential vector.

- 2^{nd} **test case:** For an axi-symmetric current density, the z component of the magnetic field B can be directly derived from Ampere's law, Eq. 2.25

  $$\frac{\partial B_z}{\partial y} = -\mu_0 j_x.$$

  There is thus no need to solve any equation for the magnetic field. The boundary conditions for the 2^{nd} case are presented in Table 3.6.

3.3.3 Numerical results

Velocity

As expected, in the absence of the electromagnetical effects both test cases deliver identical velocity fields, see Fig 3.12. As shown, after entering the inlet nozzle, the shielding gas continues directly towards the outlet, avoiding the region below the cathode tip. The velocity magnitude is of the same order as the inlet velocity profile.

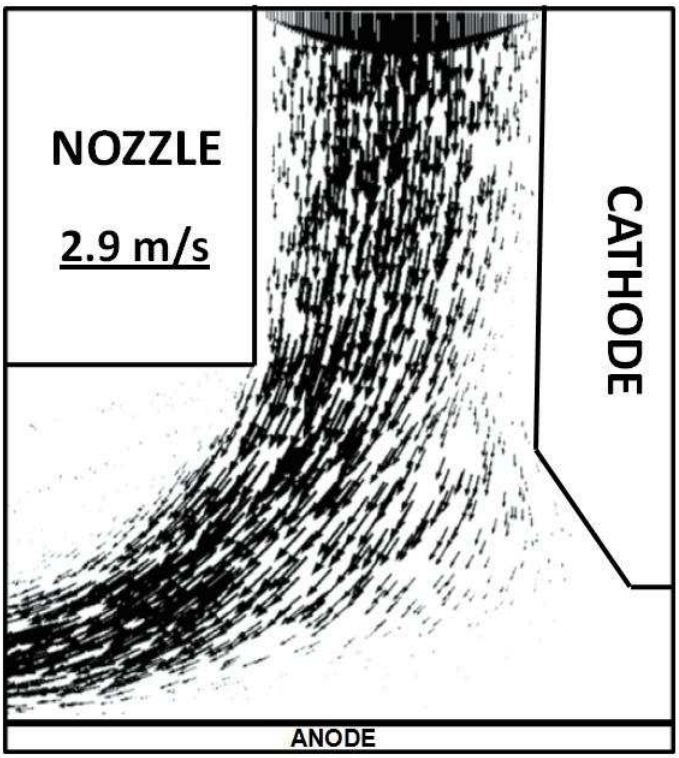

Figure 3.12: Velocity distribution inside the domain without electromagnetic forces.

When the electromagnetical effects are activated, the velocity field is shifted under the cathode tip and the flow is accelerated in this region due to the Lorenz force, see Fig. 3.13. As it can be seen, the qualitative behavior is the same for both test cases. That is in the region close to the cathode tip, the fluid flows inward and downward towards the anode surface. Due to the presence of the stagnation effects at the anode surface, the fluid is deflected and directed towards the outlet. From Fig. 3.13, it can also be observed that for the considered configuration, the inlet and outlet boundary conditions do not seem to have a significant effect on the velocity distribution in the plasma column. That is clearly indicated by the maximum velocity magnitudes of 160 [m/s] and 70 [m/s] obtained for two test cases, compared to the inlet average velocity of 2.36 [m/s].

The presence of the ceramic nozzle does not have a profound effect on the results either. This qualitative behavior is consistent with the findings of Tsai and Kou [24].

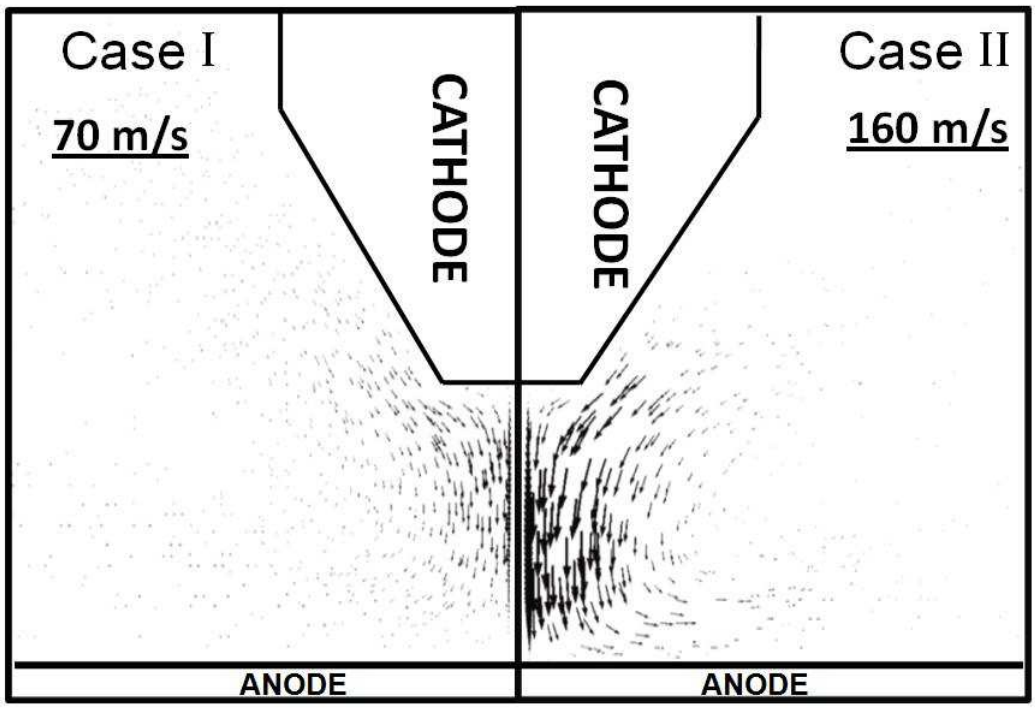

Figure 3.13: The velocity distribution with electromagnetic forces for the two cases. The velocity field is zoomed near the cathode tip.

For a better quantitative analysis of the two cases, the velocity profiles are now compared along the symmetry axis and in radial direction, see Figs. 3.14 and 3.15, respectively. Along the symmetry axis, the velocity profiles diverge almost immediately, with the maximum difference of 50% in magnitude obtained. Similar deviation in the velocity profile is observed in the radial direction. Though sufficiently away from the symmetry axis ($\approx 4mm$) both solutions approach the same value.

Temperature

The temperature distribution for both test cases is shown in Figure 3.16. As in the case of velocity field, the qualitative behavior of the temperature distributions is the same. As a result of the strong radially outward flow that was presented above, a bell-shaped arc has been formed [24]. In both cases, the maximum temperature of 22000 K is attained on the symmetry axis close to the cathode tip. The calculated isotherms for the temperatures of 10000 and 12000 K are in a relatively good agreement. This can be explained by the fact that sufficiently away from the symmetry axis the velocities for both test case approach each other, as shown in Fig. 3.15. For

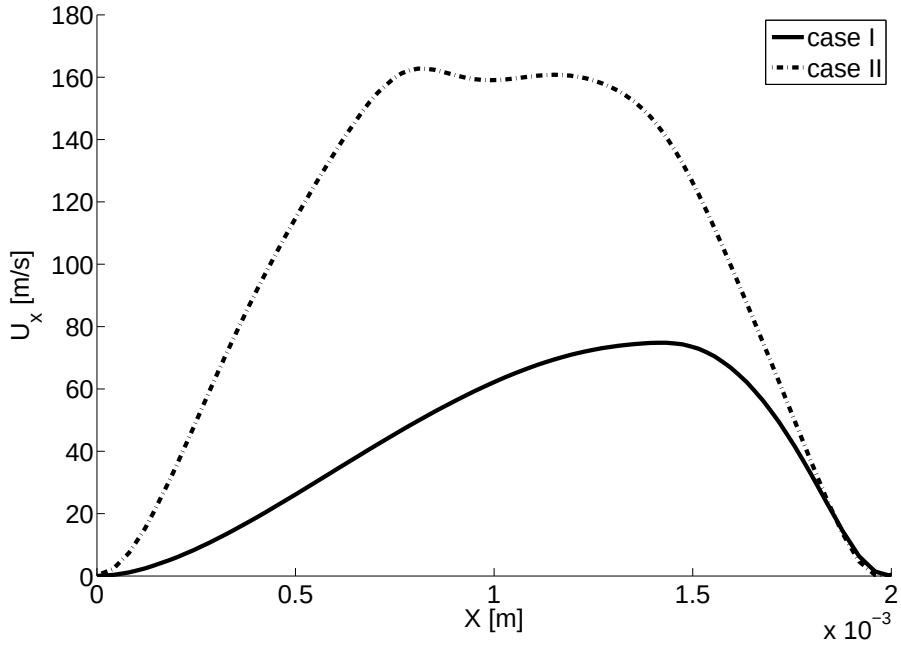

Figure 3.14: Velocity evaluated along the symmetry axis for both test cases. Here $x = 0$ represents the anode surface and $x = 2$ mm represents the tip of the cathode.

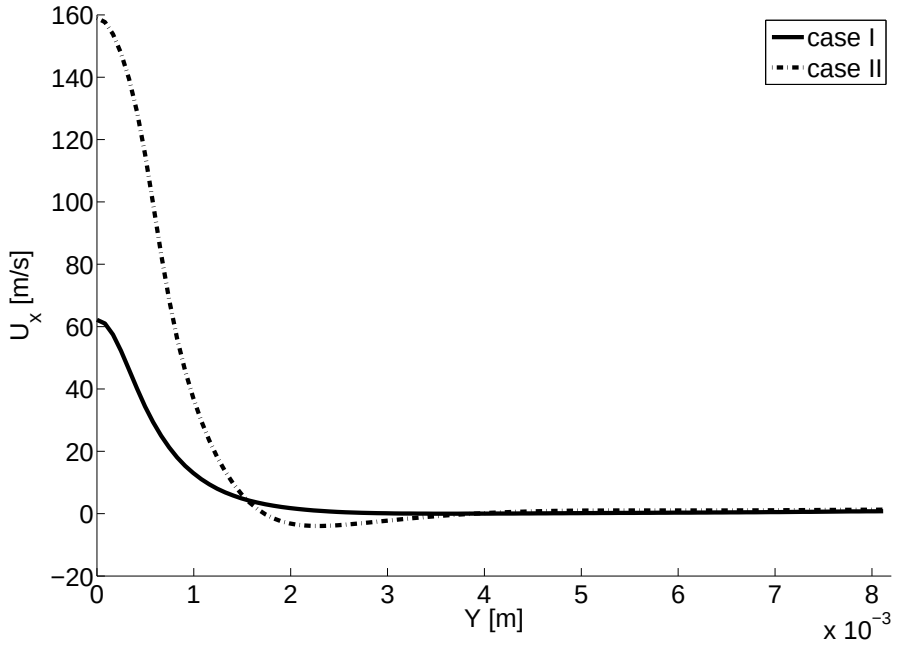

Figure 3.15: Radial distribution of the x-velocity component for both test cases evaluated at $x = 1$ [mm].

the rest of the isotherms the deviation is significant. The isotherms for the first case are clustered closer to the cathode tip, while for the second case,

the isotherm are elongated along the symmetry axis. This difference could be explained by the convection effects, that are stronger in the second case due to higher velocity field.

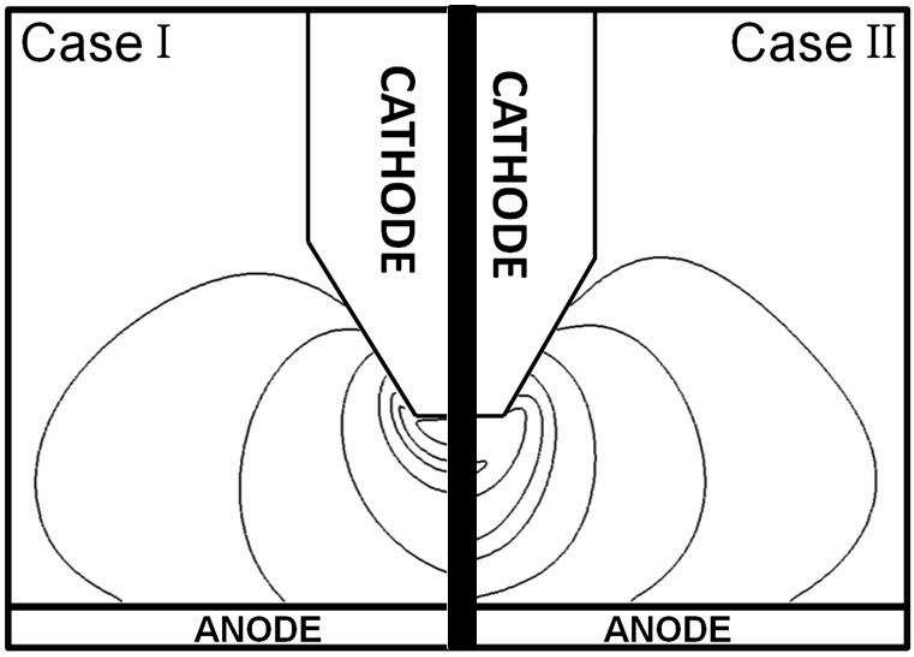

Figure 3.16: From large radius to small radius, the isotherms correspond to 10000, 12000, 14000, 16000, 18000, 20000 and 22000 K. The temperature contours are zoomed near the cathode tip.

To summarize, the comparison of the chosen two test cases revealed a clear deviation in the results. This is due to the way the magnetic field B is calculated.. The exact nature of this problem is currently not fully understood and still under investigation.

Chapter 4

Conclusions and future work

In this work a simulation tool that is valid within the field of tandem arc welding (unsteady, three dimensional thermal plasma flow) has been developed. This tool is based on the open source CFD package OpenFOAM. The tool is fully 3D, accounts for the complex interaction between the flow and the electromagnetic field, and accurately represents the strong dependence of the flow on the thermophysical properties of the plasma.

The validation of the electromagnetic part of the tool has been done separately using a problem with a known analytical solution. A good agreement between an analytic and numerical results was obtained. In addition, various boundary conditions for the electromagnetic potential have been evaluated. A good agreement between the analytic and numerical solutions was observed in the case when Dirichlet boundary condition for the magnetic potential vector was used at a far distance from the conductor representing the plasma.

The complete simulation tool was validated using a tungsten inert gas single arc problem [24]. Two methods of computing the magnetic field have been tested, based on the electric and magnetic potentials, respectively. Qualitatively, similar behavior was observed. In both cases a characteristic bell-shaped temperature profile was obtained and a high velocity jet directed towards the welded surface was formed. Upon reaching the stagnation zone, this jet is being radially deflected towards the outlet. A quantitative analysis of the results was performed by comparing the x-velocity component along the symmetry axis. This comparison revealed a 50% disagreement in the maximum value. A better agreement with the results of Tsai [24] was obtained in the case when the magnetic field was derived directly from the Amper's law. Currently, this differences in the results are not completely understood and are still under investigations.

Future work points in two directions from the current stand. First of all the disagreement in the results for two representations of the magnetic field has to be thoroughly studied. Next, one should continue towards the complete tandem arc problem. For this purpose a tilted cathode geometry

has to be introduced and the capability to simulate MAG welding has to be added to the tool. At some stage, the accurate representation of the sheath layers, solution of the heat and electromagnetic equations inside the electrodes, as well as the dynamics of the droplet and welding pool have to be also included in the simulation tool.

References

[1] Maecker H. and Finkelburg W.: *Elektriche Bogen und thermisches plasma.* Handbuch der Physik, 22: p. 244-254, 1957

[2] Pfender, E. *Electric arcs and arc gas heaters.* Gaseous Electronics, 1(5), pp. 291- 298, 1978

[3] Guile A.E. *Electric arcs : their electrode processes and engineering applications.* IEE Proc, 131, pp. 450-480, 1979.

[4] Jönsson P.G. *Matematical models of transport phenomena associated with arc welding process.* sci .Eng., 2, 1977

[5] Wendelstorf J.: *Ab initio modelling of thermal plasma gas discharges (electic arcs)*, Dissertation, TU-Braunschweig, 2000

[6] Braginskii S.I.: *Transport processes in a plasma*, Reviews of plasma physics (M A Leontovich, ed.), Vol. 1, Consultants Bureau, New York, 1965, pp. 205311.

[7] Vilsmeier F.: *Laserstreuung und Stromtransport im Argon-Bogenplasma*, Dissertation, TU München, 1982.

[8] Ramirez M. A., Trapaga G. and McKellliget J.: *A comparison between two different numerical formulations of welding arc simulation* Modelling Simul. Mater. Sci. Eng. 11, pp. 675-695, 2003

[9] McKellliget J. and Szekely J.: *Heat transfer and fluid flow in the welding arc* Metall.Trans 17A, pp. 1139-1148, 1986

[10] Weast R. C.: *CRC Handbook of Chemistry and Physics*, CRC Press, Cleveland, OH, 1975

[11] Hsu K.C., Etemadi K. and Pfender. E.: *Study of the free burning high intensity argon arc* J.Appl. Phus, 54, pp. 1293-1301, 1983

[12] Lago F., Gonzales J.J., Freton P. and Gleizes A.: *A numerical modeling of an electric arc and its interaction with the anode : part I* , J. Phys. D: Appl Phys. 37, pp. 883-897, 2004

[13] Delalondore C. : *Modélisation aérothermodynamique d'arcs électriques á forte intensité avec prise en compte du déséquilibre thermodynamique local et du transfert thermique á la cathode*, Thése de doctorat,de l'Université de Rouen, 1990

[14] Kaddani A., Delalondre C., Simonin O. and Minoo H.: *Thermal and Electrical Coupling of Arc Electrodes* High Temp. Chem. Processes 3, pp. 441-448, 1994

[15] Douce A.: *Modélisation 3-D du chauffage d'un bain métallique par plasma d'arc transféré. Application un racteur axisymétrique*, Thése d'Université - rapport EDF HE-26/99/027A - HE-44/99/043A, 1999

[16] Kaddani A., Zahrai S., Delalondore C., Simonin O.: *3D modeling of unsteady high pressure arcs in argon*, J. Phys. D:Appl Phys. 28, pp. 1-12, 1995

[17] Freton P, Gonzalez J. J., Gleizes A. : *Comparison between a two and a three-dimesional arc plasma configuration*, J. Phys. D:Appl Phys. 33, 2442-2452, 2000

[18] Jasak H.: *Error Analysis and Estimation for Finite Volume Method with Applications to Fluid Flow*, Ph. D. Thesis, London University and Imperial College of Science, Technology and Medicine, London, 1996

[19] Versteeg H. K. and Malalasekera W.: *An Introduction to Computational Fluid Dynamics*, Prentice Hall, London, 1995

[20] Tournier J-M. P. and El-Genk M.S.: *Properties of noble gases and binary mixtures for closed Brayton Cycle applications*, Energy conversion and Management, Science Direct, December 2007

[21] Boulos M.I., Fauchais P. and Pfender E.: *Thermal Plasmas, Fundamentals and Applications*, Vol. 1, Plenum Press, New York, 1994

[22] Owens E. and Thodos, G.: *Thermal-conductivity-reduced-state correlation for the inert gas*, AIChE J, 1957

[23] Fersiger J.H and Peric M.: *Computational methods for fluid dynamics*, Springer Verlag, Berlin-New York, 1995

[24] Tsai M.C. and Sindo Kou: *Heat transfer and fluid flow in welding arcs produced by sharpened and flat electrodes*, Int. J. Heat mass transfer, Vol.33 No.10, pp. 2089-2098, Great Britain, 1990

[25] Patankar S.V.: *Numerical heat transfer and fluid flow*,Hemisphere Publishing Corporation, 1981

[26] Modest M. : *Radiative Heat Transfer*, McGraw-Hill, New York, 1993

[27] Gleizes A., Gonzalez J.J. and Freton P.: *Thermal plasma modeling*, J. Phys. D: Appl Phys, 38, pp. 153-183, 2005

[28] Baudry C. : *Contribution à la modélisation instationnaire et tridimensionnelle du comportement dynamique de I' arc dans une torche de projection plasma* , Ph. D. Thesis, Université de Limoges, 2003

[29] Haddad G.N. and Farmer A.J.D : *Temperature measurements in gas tungsten arcs*, Welding J, 64,pp. 339-342, 1985

[30] Lowke J. J.: *Simple theory of free burning arcs*, J. phys. D: appl. Phys., 12, pp. 1873-86, 1979

[31] Trautz M. and Binkele H.E: *Viscosity, heat conductivity and diffusion in gaseous mixture- VIII: the viscosity of hydrogen, helium, neon and argon, and their vinary mixtures*, Ann Phys, 5(5), pp. 561-80, 1930.

[32] Watson H.E. and Paranjpé G.R.: *Some experements on the cathode fall. Part I: In Neon and Helium*

[33] Delalondre C., Zahrai S. and Simonin O.: *Turbulence Modelling in Electric Arc* Rapport EDF HE-44/94/020A, 1994

[34] Matthew N. O. Sadiku: *Numerical techniques in eletromagnetics*, Second Eddition, CRC Press LLC, Florida, 2000

[35] Choo R., Szekely J. and Westhoff R.C.: *Modeling the welding arc*, Metall. Mater. Trans. B, 23, pp. 357-69, 1992

[36] Lee Y.S. and Na S.J.: *A numerical analysis of a stationary gas tungsten welding arc considering various electrode angles* Suppl. Weld J., pp. 269-79, 1996

[37] Goodarzi M., Choo R. and Toguri J.M.: *The effect of the cathode tip angle on the GTAW arc and weld pool: I. Mathematical model of the arc* , Journal of Physics D: Applied Physics, Vol 30, Number 19, pp. 2744-2756, 1997

[38] Lowke J., Morrow R., Haidar J. and Murphy A.B.: *Prediction of 'Gas Tungsten Arc Welding' Properties in Mixtures of Argon and Hydrogen* IEEE Trans. Plasma Science, 25, pp. 925-930, 1997

[39] Ushio M. , Tanaka M. and Wu C.S.: *Analysis of the TIG welding arc behaviour*, Trans. JWRI, p25 921, 1996.

[40] Lowke J. and Morrow R.: *A One-dimensional Theory for the Electrode Sheaths of Electric Arcs*, J. Phys. D: Appl. Phys. 26, 634-642, 1993.

[41] Tanaka M., Terasaki H., Ushio M. and Lowke J.: *A unified numerical modeling of stationary tungsten-inert-gas welding process* Metall. and Mater. Trans. A, 33A, pp.2043-2052, 2002

[42] Delandore C., Douce A., Gonzales M., Gleizes A., and Guillot J.B. Proc. 14th Int. Symp. Plasma Chem. ed M Hrabovsky, Konrad and Kopecky, Vol 1, pp. 321, 1999

[43] Hu J. and Tsai L.H.: *Effects of current on droplet generation and arc plasma ingas metal welding*, J. Appl Phys, 2006

[44] Verteeg H.K. and Malalasekera W.: *An introduction to computational fluid dynamics. The finite volume method*, Printice Hall, 1995

[45] Hsu K.C. and Pfender E.: *Two-temperature modeling of the free-burning, high-intensity arc*, J. Appl. Phys. 54, pp. 4359-4366, 1983

[46] Lancaster J.F: *The physics of welding*, Phys. Technol., Vol 15, 1985

[47] Petrov V.: *Article: "ArticleElectric arc"*, Great Soviet Encyclopedia, 1990

[48] Choquet I., Degond P. and Lucquin-Desreux B.: *A hearchy of diffusion models for partially ionized plasmas*, Descrete and Continuous Dynamical System Series B, Vol 8, 4, pp. 735-772, 2007

[49] Choquet I. and Lucquin-Desreux B.: *Hydrodynamic Limit for an arc discharge at atmospheric pressure*, Journal of Statical Physics, Vol. 119, 112, pp. 197-239, 2005

[50] Rat V., Pascal A., Aubreton J., Elchinger M. F., Fauchais, P. and Lefort A.: *Transport properties in a two-temperature plasma: Theory and application*, Physical Review E (Statistical, Nonlinear, and Soft Matter Physics), Vol 64, 2, August 2001

[51] Rat V., Pascal A., Aubreton J., Elchinger M.F., Fauchais P. and Vacher D.:*Transport coefficients including diffusion in a two-temperature argon plasma* Journal of Physics D, 35 pp. 981-991, 2002

[52] Gleizes A., Gonzalez J. J., Razafinimanana M. and Robert T.: *Influence of radiation on temperature field calculation in SF6 arcs*, Plasma Sources Sci. Technol., Vol 1, p. 135, 1992

Appendix A

Details on the thermodynamic and transport properties

Due to high temperature range, the distributions of the thermophysical and transport properties were assembled from both kinetic theory and experimental values. In this section the details on this assembly process are given. The comparison of the kinetic and experimental values for the overlapping domain of validity is also presented.

A.1 Density

There are several types of gas models with slightly different behavior. For example ideal gases (single species), real gases (single species) and plasmas (mixture).

The ideal gas law reads

$$PV = nRT \quad \text{or} \quad \rho = \frac{P}{RT} \tag{A.1}$$

where P is the pressure, V the volume, T the temperature, n the number of moles of gas present, R the universal gas constant (8.31441 $JK^{-1}mol^{-1}$), and ρ is the density.

This model applies to light gases, such as argon, away from their critical point, see Table A.1 for critical values for argon. In other words it applies to gases with a small density compared to the critical density, allowing to model the atoms/molecules as hard sphere.

The real gas laws account for the compressibility of molecule (soft sphere) by adding terms to describe attractions and repulsions between molecules. Real gas laws have been determined empirically, or is based on a conceptual model of molecular interactions, or from statistical mechanics. One of the well-known real gas laws is the *virial equation of state*, that is based on

the definition of a compressibility factor Z, defined as

$$Z = \frac{PV}{RT}.$$

When Z goes to one the real gas model reduces to the ideal gas model.

At low temperatures (200 to 500 K) and pressure close to the atmospheric (as considered in this work), the argon gas has a compressibility factor less than one. The compressibility factor can be written in the form of the power series

$$Z = 1 + B/V + C/V^2 + ...$$

where B and C are the second and the third virial coefficients, respectively.

This equation can also be written as a second-order polynomial in the molar density of the form

$$\rho = \hat{\rho} + B\hat{\rho}^2 + C\hat{\rho}^3 \tag{A.2}$$

where $\hat{\rho}$ is the molar density obtained from the *ideal gas law*. The density of argon gas is calculated using the *virial equation of state* in [20]. This calculation requires the knowledge of the second and third virial coefficients which are functions of temperature and characteristic of the interactions between the particles. Note that Eq. A.2 is accurate at least up to the critical density [20], see Table A.1.

.

In this study, the formulation for the virial coefficients that were presented in the work of Tournier and El-Genek [20] is used. Thus the second virial coefficient B is represented by the following expression

$$B = V^* \cdot [-102.6 + (102.732 - 0.001 \times \theta - 0.44/\theta^{1.22}) \times \tanh(4.5\sqrt{\theta})] \tag{A.3}$$

where $V^* = RT_{cr}/P_{cr}$ and $\theta = T/T_{cr}$ denotes the reduced temperature. The critical value for the temperature T_{cr} and pressure P_{cr} are given in the Table A.1.

The third virial coefficient C is given by

$$C = V^{*^2} \cdot [0.0757 + (-0.0862 - 3.6 \times 10^{-5} \times \theta + 0.0237/\theta^{0.059}) \times \tanh(0.84 \times \theta)]. \tag{A.4}$$

$T_{cr}[K]$	$P_{cr}[kPa]$	$V_{cr}[m^3/mole]$	$\rho_{cr}[kg/m^3]$
150.7	4863	74.59e-6	535.6

Table A.1: Fundamental and critical properties of argon gas.

In the present work the temperature varies from 300 up to 30000 K. When the temperature of the gas reaches the ionization point, a part of its particles become ionized. Then, as mentioned earlier, the gas gets a multicomponent plasma and the virial equation of state does not apply to this mixture. Therefore another description of the state of matter under a given set of physical conditions has to be employed. In the current work, the kinetic theory of the gas is instead used.

That is the experimental data for the low temperatures was combined together with the data obtained from kinetic theory for the higher temperatures. It was also checked that these data do overlap correctly.

First, the density in the range from 200K up to 5000K was studied. Here the density obtained with the Eq. A.2 is in a good agreement with the kinetic theory data, see Fig A.1(a).

As it can be seen from Figure A.1(b), the extrapolation (above 1400 K) of the experimental data and the data from the kinetic theory are in good agreement before the first ionization takes place. When the first ionization gets significant the argon gas gets a plasma mixture that can no longer be described by a single species real gas model.

A.2 Dynamic viscosity

Tournier and El-Genk [20] showed that the viscosity of pure noble gases can be expressed as a function of the temperature and the density

$$\mu = \mu^0(T) + (1 - \frac{1}{2.3})\mu_{cr} \cdot \psi_\mu\Big(\frac{\rho}{\rho_{cr}}\Big) \tag{A.5}$$

where μ_{cr}, ψ_μ and μ_0 are the critical viscosity, reduced excess viscosity and viscosity of the dilute gas, respectively. The critical viscosity is calculated in [22] using the relationship proposed by Trautz [31]

$$\mu^*_{cr} = b\frac{\sqrt{MT_{cr}}}{V_{cr}^{2/3}}.$$

Here, the constant $b = 0.204 \cdot 10^{-7}$ is determined from the critical viscosity values [20], $M = 0.039948$ [kg/mole] is the argon gas molecular weight and the critical molar volume V_{cr} is listed in Table A.1. In Eq. A.5 the reduced excess viscosity is expressed as a function of the reduced density [20]

$$\psi_\mu\Big(\frac{\rho}{\rho_{cr}}\Big) = 0.221\frac{\rho}{\rho_{cr}} + 1.062\Big(\frac{\rho}{\rho_{cr}}\Big)^2 - 0.509\Big(\frac{\rho}{\rho_{cr}}\Big)^3 + 0.225\Big(\frac{\rho}{\rho_{cr}}\Big)^4.$$

The viscosity of the dilute gas in Eq. A.5, $\mu^0(T)$, is defined by the following correlation

$$\mu^0(T) = A_\mu(T - T_\mu)^n$$

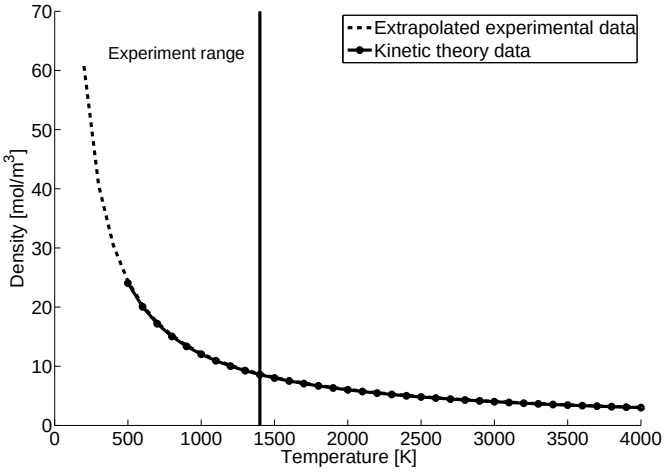

(a) Before ionization.

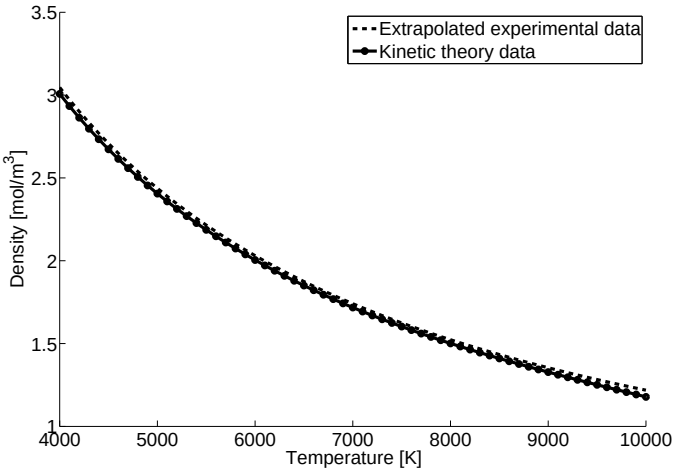

(b) First ionization

Figure A.1: Density of argon gas versus temperature for overlaping domain of validity of the two sets of data.

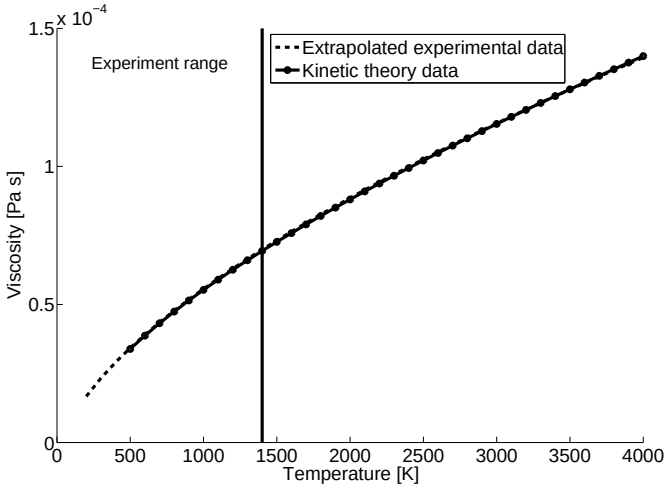

(a) Before ionization.

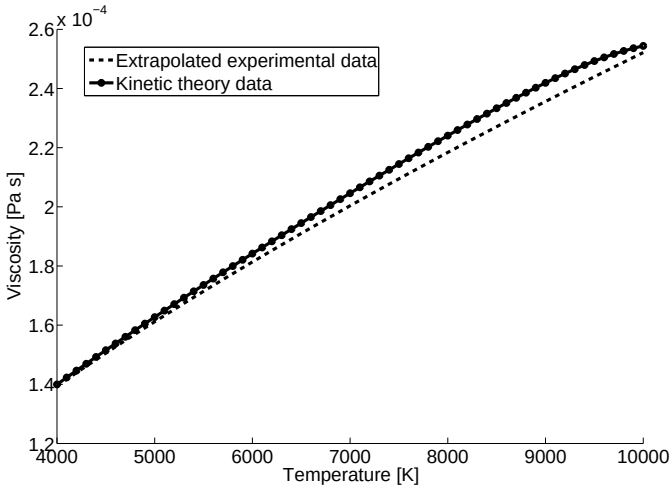

(b) First ionization

Figure A.2: Viscosity of argon gas versus temperature for overlaping domain of validity of the two sets of data.

where $n = 0.63977$ denotes the exponent for the argon gas. The values of the viscosity correlation coefficients are $A_\mu = 6.9891 \cdot 10^{-7}$ and $T_\mu = 65.7$ [K] [20].

A.3 Thermal conductivity

A semi-empirical expression for the thermal conductivity of dense gases was also developed in the work of Tournier and El-Genk [20]

$$\lambda(T,P) = \lambda^0(T) + (1 - \frac{1}{2.94})\lambda^*_{cr} \times \psi_k(\frac{\rho}{\rho_{cr}}) \tag{A.6}$$

where λ^0, λ^*_{cr} and ψ_k are the thermal conductivity, critical thermal conductivity and reduced excess thermal conductivity, respectively. The thermal conductivity of the pure, dilute gases is calculated accurately in terms of the dynamic viscosity using the kinetic-theory relationship

$$\lambda^0(T) = \frac{15}{4}\frac{R}{M}\mu^0 = \frac{15}{4}\frac{k}{m}\mu^0$$

where k is the Boltzmann constant ($1.380662 \cdot 10^{-23} J/K$) and m is the mass of one gas molecule ($m = M/N_A kg$).

An expression for the critical thermal conductivity was developed by Tournier and El-Genk [20] using the approach of Owens and Thodos [22]

$$\lambda^*_{cr} = 0.304 \cdot 10^{-4} \frac{T_{cr}^{0.277}}{M^{0.465}(0.291 \cdot V^*)^{0.415}}.$$

The empirical relationship for the reduced excess thermal conductivity used in Eq. A.6 was obtained in [20] from the least square approximation of compiled experimental data is given as

$$\psi_k(\rho/\rho_{cr}) = 0.645 \cdot (\rho/\rho_{cr}) + 0.331 \cdot (\rho/\rho_{cr})^2 + 0.0368 \cdot (\rho/\rho_{cr})^3 - 0.0128 \cdot (\rho/\rho_{cr})^4.$$

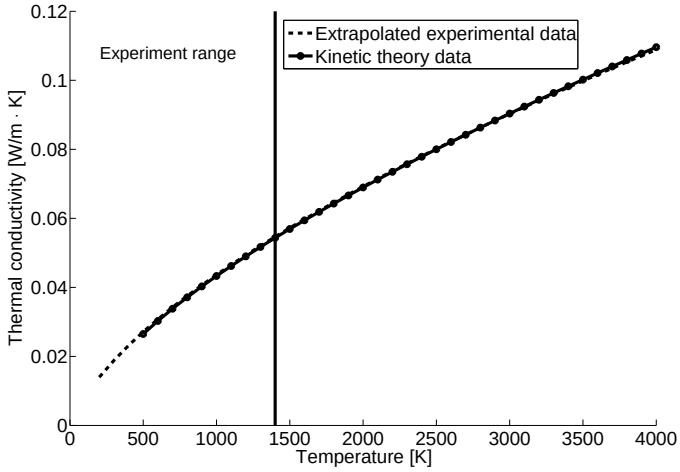

(a) Before ionization.

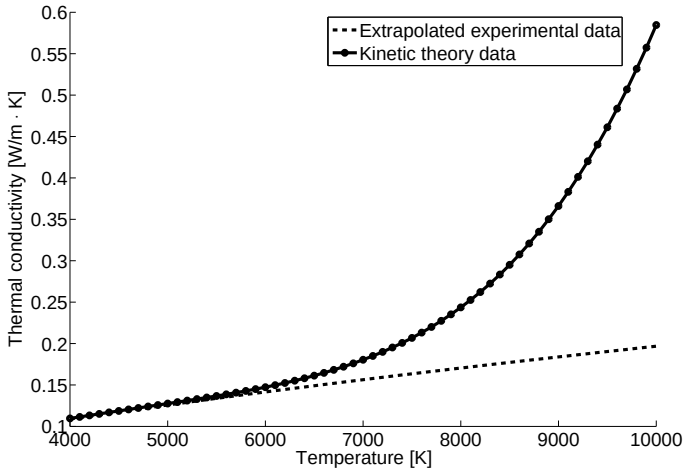

(b) First ionization

Figure A.3: Thermal conductivity of argon gas versus temperature for overlaping domain of validity of the two sets of data.

A.4 Enthalpy and specific heat

The thermodynamic properties such as the enthalpy and the heat capacities were calculated at low temperatures using fundamental thermodynamic relationships [20]. Then the enthalpy equation reads

$$\hat{H}(T,P) = \hat{H}^0(T_0) + \hat{C}_p^0(T - T_0) + \hat{\rho}RT[(B - T\frac{dB}{dT}) + \hat{\rho}(C - \frac{T}{2}\frac{dC}{dT})]. \quad \text{(A.7)}$$

Here B and C are the second and third virial coefficients given by Eqs A.3 and A.4, respectively. The ideal value of specific heat capacity at constant pressure for a monoatomic dilute gas is denoted by $\hat{C}_p^0 = 5R/2$ and $H^0(T_0) = 0\ [J/mol]$ is the reference ehthalpy. The specific heat capacity at constant pressure is then calculated as

$$\begin{aligned} \hat{C}_P &= [\frac{\partial \hat{H}}{\partial T}]_P \\ &= \hat{C}_P^0 + \hat{\rho}[(B - T\frac{dB}{dT} - T^2\frac{d^2B}{dT^2}) + \hat{\rho}(C - \frac{T^2}{2}\frac{d^2C}{dT^2})] \\ &\quad + RT[(B - T\frac{dB}{dT}) + \hat{\rho}(2C - T\frac{dC}{dT})] \times [\frac{\partial \hat{\rho}}{\partial T}]_P \end{aligned} \quad \text{(A.8)}$$

where

$$[\frac{\partial \hat{\rho}}{\partial T}]_P = \frac{(\hat{\rho} + B\hat{\rho}^2 + C\hat{\rho}^3)/T + \frac{dB}{dT}\hat{\rho}^2 + \frac{dC}{dT}\hat{\rho}^3}{1 + 2B\hat{\rho} + 3C\hat{\rho}^2}.$$

The values for the coefficients B, C and their derivatives are obtained from Eqs. A.3 and A.4, respectively.

The derivatives for the second coefficient virial coefficient B are given by

$$\begin{aligned} \frac{dB}{dT} = V^* \cdot [&(-0.001/T_{cr} + 0.5368 \cdot T_{cr}^{1.22} \cdot T^{-2.22}) \cdot \tanh(4.5 \cdot \sqrt{\theta}) + \\ &(102.732 - 0.001 \cdot \theta\ - \frac{0.44}{\theta^{1.22}}) \cdot \frac{2.25}{\sqrt{T_{cr} \cdot T}} \cdot (1 - \tanh^2(4.5 \cdot \sqrt{\theta}))], \end{aligned}$$

$$\begin{aligned} \frac{d^2B}{dT^2} = V^* \cdot [&(-1.1917 \cdot T_{cr}^{1.22} \cdot T^{-3.22}) \cdot \tanh(4.5 \cdot \sqrt{\theta}) + \\ &2 \cdot (-0.001/T_{cr} + 0.5368 \cdot T_{cr}^{1.22} \cdot T^{-2.22}) \cdot \tanh(4.5 \cdot \sqrt{\theta}) \cdot (1 - \tanh(4.5 \cdot \sqrt{\theta}) + \\ &+ (102.732 - 0.001 \cdot \theta - \frac{0.44}{\theta.^{1.22}}) \cdot (\frac{-1.1250}{T_{cr}^{0.5} \cdot T^{1.5}} \cdot \\ &(1 - \tanh^2(4.5 \cdot \sqrt{\theta})) - \frac{10.1250}{T_{cr} \cdot T} \cdot \tanh(4.5 \cdot \sqrt{\theta}) \cdot (1 - \tanh^2(4.5 \cdot \sqrt{\theta})))] \end{aligned}$$

and the derivatives for the third virial coefficient C are

$$\frac{dC}{dT} = V^{*^2} \cdot [(-3.6^{-5} \cdot T_{cr}^{-1} - 0.0014 \cdot T_{cr}^{0.059} \cdot T^{-1.059}) \cdot \tanh(0.84 \cdot \theta) + (-0.862 - 3.6^{-5} \cdot \theta + 0.0237 \cdot \theta^{-0.059}) \cdot \frac{0.84}{T_{cr}} \cdot (1 - \tanh^2(0.84 \cdot \theta))],$$

$$\frac{d^2C}{dT^2} = V^{*^2} \cdot [0.0015 \cdot T_{cr}^{0.059} \cdot T^{-2.059} \cdot \tanh(0.84 \cdot \theta) + 2 \cdot (-3.6^{-5} \cdot T_{cr}^{-1} - 0.0014 \cdot T_{cr}^{0.059} \cdot T^{-1.059}) \cdot \frac{0.84}{T_{cr}} \cdot (1 - \tanh^2(0.84 \cdot \theta)) + (-0.862 - 3.6^{-5} \cdot \theta + 0.0237 \cdot \theta^{-0.059}) \cdot \frac{-1.4112}{T_{cr}^2} \cdot \tanh(0.84 \cdot \theta) \cdot (1 - \tanh^2(0.84 \cdot \theta))].$$

Again, the extrapolation of the experimental data diverges from the data from kinetic theory when the first ionization becomes significant. See Fig A.4(b) and A.5(b) for heat capacity and enthalpy, respectively.

The enthalpy and the heat capacity values that are calculated using Eq. A.7 and A.8, respectively, have been supplemented with tabulated data that are obtained from kinetic theory.

A.5 Plasma radiation

Due to very high temperatures of thermal plasma, radiation is an important phenomenon which has to be accounted for. Qualitatively, radiation has three two effects [27]:

- in the hottest regions, radiation is the dominant energy loss term,
- in the outer regions, radiation is a signifacant part of the energy transfer within the plasma.

The radiative transfer equation is given in the following simple form, along one direction in a nonscattering plasma with a refractive index equal to one [26] :

$$\frac{dI_\nu}{dr} = \underbrace{\epsilon_\nu}_{\text{emmision}} - \underbrace{I_\nu K'_\nu}_{\text{absorbtion}} \tag{A.9}$$

where the intensity $I_\nu(\vec{r}, \vec{s})$ $[W\ m^{-2}\ sr^{-1}]$ is the radiative power per unit solid angle and per unit apparent surface, K'_ν is the absorbtion coefficient per unit length at frequency ν and $\epsilon_\nu = K'_\nu B_\nu$ $[W\ m^{-3}\ sr^{-1}]$ represents the emmision coefficient, that is the power at frequency ν radiated by a unit volume of the plasma per unit solid angle.

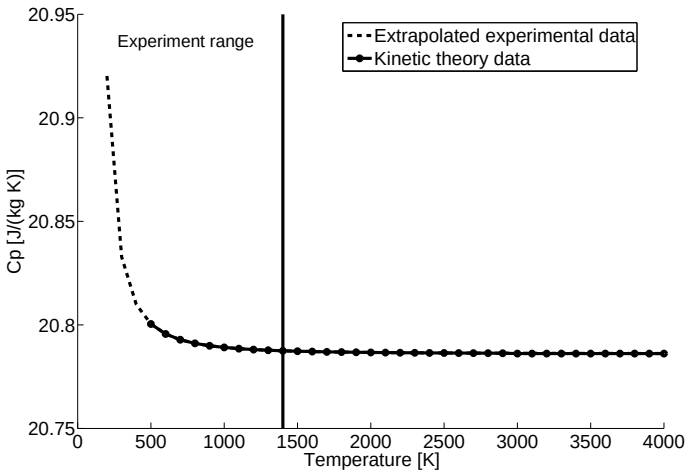

(a) Before ionization.

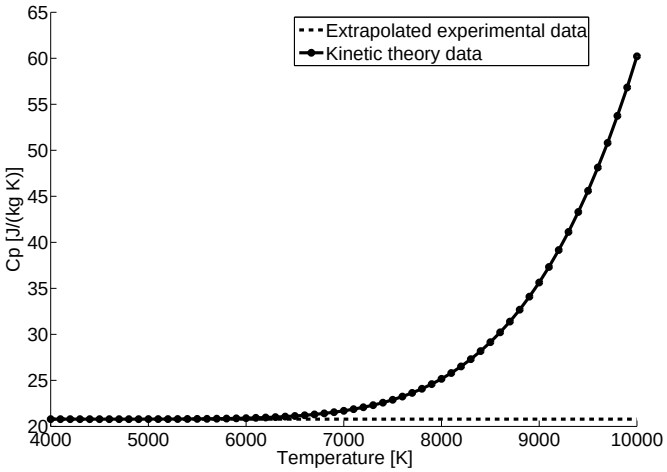

(b) First ionization

Figure A.4: Heat capacity of argon gas at constant pressure versus temperature for overlaping domain of validity of the two sets of data.

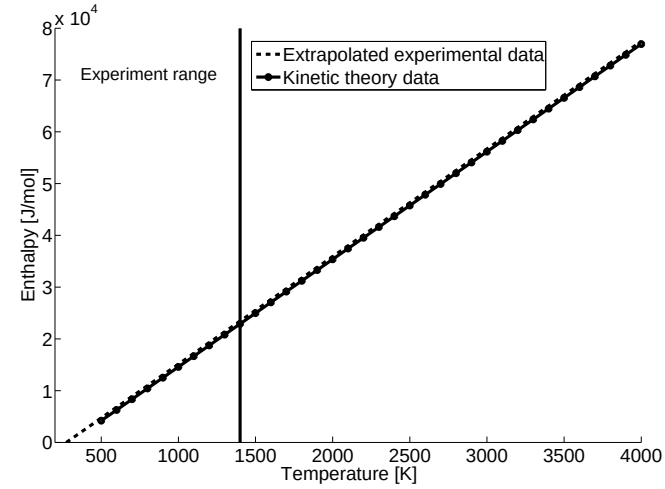

(a) Before ionization.

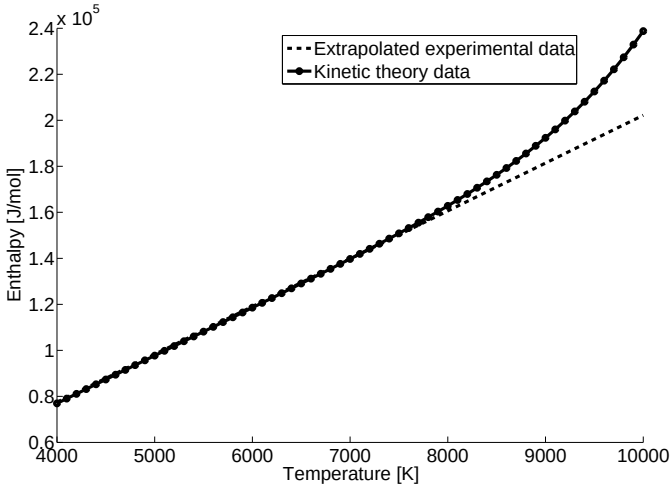

(b) First ionization

Figure A.5: Enthalpy of argon gas versus temperature for overlaping domain of validity of the two sets of data.

In the local thermodynamic equlibrium (LTE), Kirchoff's law is valid for a given wavelength and a given temperature

$$\frac{\epsilon_\nu}{K'_\nu} = B_\nu(T,\nu) = \frac{2h\nu^3}{c^2(e^{h\nu/kT}-1)} \tag{A.10}$$

with B_ν denoting black-body radiation, c the speed of light and h the Plank constant.

Unfortunately even for the simple Eqn. A.9 the computation of the total radiation transfer is a complicated task. This is due to the fact that the radiation intensity and its divergence are rapidly varying functions of the frequency. Large computational effort is therefore required for a rigorous treatment of the radiation heat transfer terms in plasma modelling.

A number of simplified approaches are available. In this work, the NEC (net emission coefficient) model has been used, which results in computing the net radiation ϵ_N[11] in the center of the isothermal sphere[12]

$$\epsilon_N = \int_0^\infty B_\nu K'_\nu exp(-K'_\nu R_p) d\nu \tag{A.11}$$

where R_p is the radius of the sphere. For further details on radiation transfer and derivation of the net emission coefficient, see Gleizes *et al.* [27] and Rat *et al.* [50],[51].

[11] Net means the difference between emission and absorption, i.e. the divergence of the radial intensity

[12] The assumption of constant temperature seems to be very restrictive, but it has been demonstrated that it is a valid for central region of thermal plasmas [52]

Appendix B

Numerical solution and algorithm

The system of Eqs. 2.36-2.40 is supplemented by the constitutive relations, initial and boundary conditions has generally no analytical solution. Therefore a numerical algorithm is usually sought. In this chapter, the main features of the finite volume based numerical algorithm that is used in this work are briefly described. This is followed by the details on the discretization of the momentum, continuity, energy and Maxwell's equations. Finally, the complete algorithm is presented and its particularities are discussed.

B.1 Discretization of the transport equation

In the frame of the finite volume method, the system of Eqs. 2.36-2.40 is written in the conservative form. In the general case, when both convection and diffusion effects are present, the general transport equation is given in the following integral formulation

$$\int_{\Delta t}\Big[\underbrace{\frac{\partial}{\partial t}\int_V \rho\phi dV}_{\text{temporal derivative}} + \underbrace{\int_V \nabla\cdot(\rho U\phi)dV}_{\text{convection term}} - \underbrace{\int_V \nabla\cdot(\rho\Gamma\nabla\phi)dV}_{\text{diffusion term}}\Big]dt = \int_{\Delta t}\Big[\underbrace{\int_V S(\phi)dV}_{\text{source term}}\Big]dt. \quad \text{(B.1)}$$

Here ϕ is a tensorial property considered continuous in space, Γ is the diffusion coefficient and $S(\phi)$ is the source term.

The discretization of the transport equation B.1 will be performed term by term. The generalized form of Gauss theorem will be used throughout the discretization procedure.

B.1.1 Temporal derivative

The time derivative captures the rate of change of ϕ. We need only to handle the volume integral.

- Using the temporal variation in a point

$$\phi(t + \Delta t) = \phi(t) + \Delta t\Big(\frac{\partial \phi(t)}{\partial t}\Big)$$

  where Δt is time-step.

- Defining time levels ϕ^n and ϕ^{n-1}

$$\phi^{n-1} = \phi(t = t_{old})$$
$$\phi^n = \phi(t = t_{old} + \Delta t)$$

- Temporal derivative, first order approximation

$$\frac{\partial \phi}{\partial t} = \frac{\phi^n - \phi^{n-1}}{\Delta t}$$

- Thus the following expression is used in the volume integral approximation

$$\int_V \frac{\partial \phi}{\partial t} dV = \frac{\phi^n - \phi^{n-1}}{\Delta t} V$$

B.1.2 Convection term

Consider the terms under the convective term in Eq. B.1. Having in mind that the control volume, or simply cell, is bounded by a series of flat faces, the convective term can be transformed into a sum of integrals over all faces:

$$\int_V \nabla \cdot (\rho U \phi) dV = \int_{\partial V} dS \cdot (\rho U \phi) = \sum_f S(\rho U)_f \phi_f = \sum_f F \phi_f$$

where F represents the mass flux through the cell face f

$$F = S \cdot (\rho U)_f.$$

These fluxes have to satisfy continuity for every cell. They can be estimated using the interpolated values of U and ρ onto the face. This interpolation may introduce an error into mass flux. The calculation of these fluxes will later be discussed separately in the Section B.2.2.

The face value of the ϕ_f is calculated from the values in the cell centers. In this study it is obtained using the convection differencing scheme. The upwind differencing or 'donor cell' scheme takes into account the flow direction when determining the value at the cell face [44]

$$\phi_f = \begin{cases} \phi_f = \phi_P & \text{for } F \geq 0 \\ \phi_f = \phi_E & \text{for } F < 0. \end{cases}$$

where P denotes the center of the currently considered cell and E is the center of its neighbour cell.

B.1.3 Diffusion term

The *laplacian operator* was discretized in a similar way. It is integrated over a control volume and linearized as follows

$$\int_V \nabla \cdot (\rho\Gamma_\phi \nabla\phi) dV = \int_{\partial V} dS \cdot (\rho\Gamma_\phi \nabla\phi)_f = \sum_f (\rho\Gamma_\phi)_f S_f \cdot (\nabla\phi)_f$$

where the terms $(S \cdot \nabla\phi)_f$ and $(\rho\Gamma_\phi)$ need further treatment. Since in the current work the considered mesh is orthogonal, i.e. vector d and S in Fig. B.1 are parallel, it is possible to use the following expression [18]:

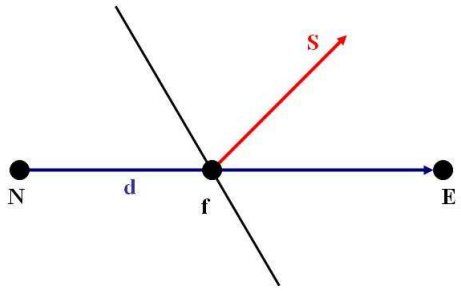

Figure B.1: An example of the non-orthogonal mesh. Here d denotes the distance between the cell centers and S is the normal on the common face.

$$S_f \cdot (\nabla\phi)_f = \mid S_f \mid \frac{\phi_E - \phi_P}{\mid d \mid}.$$

B.1.4 Source term

All terms in the equations that cannot be written as convection or diffusion terms are treated as sources. First, if the source term is non-linear with respect to ϕ, linearization is performed [18], such as

$$S(\phi) = S_u(\phi) + S_p(\phi)\phi(x).$$

When this equation is integrated over the control volume, the discretised form of the source term is obtained

$$\int_V S(\phi)dV = S_u V + S_p V \phi_P.$$

B.1.5 Boundary conditions

The solution of the general transport equation B.1 is not complete without boundary and initial conditions. The initial conditions are necessary for transient calculations in order to determine the initial state of the problem under consideration. The convection and diffusion terms require fluxes through cell faces which have to be specified at the boundary or evaluated from initial and boundary data. Most commonly, boundary conditions are:

- *Dirichlet boundary condition*: given by prescibing the value of ϕ at the boundary
- *Von Neumann boundary condition*: given by specifying the gradient of ϕ

More specifycally, in this work some physical boundary conditions that occur when solving our system of equations are:

- **Inlet.** The velocity distribution is prescribed and the surface normal gradient is set to zero for the pressure.
- **Outlet.** The pressure distribution is prescibed there. Surface normal gradient of the velocity field is set to zero.
- **Non-slip wall.** The velocitiy field is fixed to the velocity of the wall that is set to zero in our case. As convection flux through the wall is zero, the gradient of the pressure is set to zero there.
- **Thermaly isolated wall.** No heat flux going through the wall, i.e. the surface normal gradient of the temperature is zero.

B.1.6 Solution of the linear equation system

As a result of the discretisation procedure, a system of algebraic equations is obtained. These equations may be linear or non-linear. When equations are non-linear they can be linearised in some manner and then solved as for linear problems, but in an iterative or time-marching fashion.

The system of linear algebraic equations can be written in the following general form, [18]:

$$a_P \phi_P + \sum_N a_N \phi_N = Q_p$$

where P is the control volume under consideration, N stands for the neighbours of the control volume P and coefficients a accumulates all the corresponding discretization details.

The resulting algebraic system can be solved either by *direct* or *iterative* method. Direct methods provide a solution of the system in a fixed number of operations. The most popular methods of this type are: Thomas algorithm (TDMA), Gauss elimination and LU decomposition. They are appropriate for a small systems as the number of required operations increases rapidly with number of the equations, except in case of TDMA for which it increases linearly.

However, in this work an iterative method is employed. This iterative method starts from an initial solution and subsequently improves the solution until user specified error tolerance is met. In this study two methods are used: Preconditioned Conjugate Gradient (PCG) and BiConjugate Gradient (PBiCG) methods.

B.2 Solution algorithm for the pressure-velocity coupling

B.2.1 Derivation of the pressure equation

Combining the information from the preceeding sections, the complete discretization of the momentum equations is now written down. However, one thing remains to be specified, namely the pressure gradient. Note, that in our case (compressible and thermally expandable flow) the continuity equation becomes an additional constraint on the velocity field. A way to overcome this difficulty is to construct the pressure field such that velocity satisfies the continuity equation. This is done by modifying the continuity equation into an equation for the pressure [18].

Consider the discretized momentum equations in the matrix form. The momentum matrix can be decomposed into the diagonal and off-diagonal contributions. For the purposes of the derivation, the pressure gradient term will remain in the differential form. For each control volume, the dicretised momentum equation yields

$$a_P^u u_P + \sum_N a_N^u u_N = r - \nabla p \tag{B.2}$$

where a_P^u is a diagonal elements of the momentum matrix. Introduce the $H(u)$ operator, containing the off-diagonal part of the momentum matrix

and any associated r.h.s. contributions:

$$H(u) = r - \sum_N a_N^u u_N \tag{B.3}$$

Substitute (B.3) in (B.2) to obtain

$$a_P^u u_P = H(u) - \nabla p.$$

or

$$u_p = (a_P^u)^{-1}(H(u) - \nabla p) \tag{B.4}$$

Substituting the expression for u_p into the compressible continuity equation yields

$$\nabla \cdot [\rho (a_P^u)^{-1} \nabla p] = \nabla \cdot [\rho (a_P^u)^{-1} H(u)]$$

This expression is the pressure equation with the diagonal part of the discretized momentum acting as diffusivity and divergence of the velocity on the r.h.s..

B.2.2 Assembling the conservative fluxes

The pressure equation has been derived from the continuity equation and the role of the pressure is to guarantee a divergence-free velocity field. Consider the discretised form of the continuity equation [18]

$$\nabla \cdot (\rho u) = \sum_f s_f \cdot (\rho u) = \sum_f F$$

where s_f is a face area vector and F is the face flux:

$$F = s_f \cdot (\rho u)$$

Therefore, the conservative face flux should be created from the solution of the pressure equation. Substitute the expression for u from (B.4) into the flux equation, it follows:

$$F = -\rho (a_P^u)^{-1} s_f \cdot \nabla p + \rho (a_P^u)^{-1} s_f \cdot H(u)$$

Note, that a part of the above expression, $\rho (a_P^u)^{-1} s_f \cdot \nabla p$ appears during the discretization of the Laplacian, for each face. This is discretized as follows:

$$\rho (a_P^u)^{-1} s_f \cdot \nabla p = \rho (a_P^u)^{-1} \frac{|s_f|}{|d|} (p_N - p_P) = \rho a_N^p (p_N - p_P)$$

where, $a_N^p = (a_P^u)^{-1} \frac{|s_f|}{|d|}$ is equal to the off-diagonal matrix coefficient in the pressure Laplacian.

Note that in order for the face flux to be conservative, assembly of the flux must be completely consistent with the assembly of the pressure equation (e.g. non-orthogonal correction).

B.2.3 The SIMPLE algorithm

To resolve the problems associated with the non-linearities in the equations and the pressure-velocity coupling, an iterative solution strategy such as the Semi-Implicit Algorithm for Pressure-Linked Equations (SIMPLE) of Patankar and Spalding [25] for the transient problem was adopted. The discretised momentum equation include the transient term. This term is also required in the pressure correction equation. In the standard version of the algorithm the convective fluxes per unit mass F through the cell faces are evaluated from the so-called guessed velocity components. Furthermore, a guessed pressure field is used to solve the momentum equations and the pressure equation. The corrected pressure is in turn used to update the velocity field. To start the iteration process initial guesses for the velocity and pressure fields are used. As the algorithm proceeds, the aim is to progressively improve these guessed fields. The process is iterated until convergence of the velocity and pressure is achieved.

The algorithm can be summarized as follows

1. To initiate the SIMPLE calculation process a pressure field p^*, density ρ^* , thermal and transport properties are guessed.
2. An approximation of the velocity field is obtained by solving the momentum equation using the guessed pressure (or pressure from the previous iteration)

   $$a_P^u u_P = H(u) - \nabla p^*$$

   This step is called *momentum predictor*.
3. By using the guessed pressure and velocity fields, the enthalpy distribution can be obtained. The temperature distribution is obtained though the enthalpy. Thus density, thermal and transport properties can be obtained.
4. Calculation of the new pressure is based on the new velocity field and on the new density.

   $$\nabla \cdot [\rho (a_P^u)^{-1} \nabla p] = \nabla \cdot [\rho (a_P^u)^{-1} H(u)]$$

   This is called *pressure correction* step.
5. Based on the pressure solution, assemble conservative flux F

   $$F = \rho (a_P^u)^{-1} s_f \cdot H(u) - \rho a_N^p (p_N - p_P)$$

6. Repeat to convergence

B.2.4 Under-relaxation procedure

The algorithm in its base form produces a series of corrections on u and p. Unfortunately, in the above form it will diverge due to the fact that the pressure correction contains both the pressure as a physical variable and a component which forces the discrete fluxes to become conservative [44].

In order to achieve convergence some *under-relaxation* is used during the iterative process and a new, improved pressure is obtained with

$$p^{**} = p^* + \alpha_P(p - p^*)$$

where α_P is pressure under-relaxation factor. If α_P is selected equal to 1 the guessed pressure field p^* is equal to p, that is the solution of the pressure equation. A value of α_P between 0 and 1 allows to add to the guessed field an α_P fraction of the correction field p^* that is large enough to move the iterative improvement process forward, but ,at the same time, small enough to ensure stable computation [44].

The velocities also need under-relaxation. The iteratively improved velocity is obtained from

$$u^{**} = u^* + \alpha_U(u - u^*)$$

where α_U is the velocity under-relaxation factor with a value between 0 and 1. u is solution of the momentum equations and u^* presents the series of velocity approximations. The enthalpy is usually also under-relaxed for the very same reasons as pressure and velocity field. A correct choice of the under-relaxation factors α is essential for cost-effective simulations. Too large value of α may lead to oscillatory or even divergent iterative solutions and a value which is too small will cause extremely slow convergence. The optimum values of under-relaxation factor are flow dependent. Some guidelines for choosing under-relaxation are

$$\begin{aligned} 0 < \alpha_P \leq 1 \\ 0 < \alpha_U \leq 1 \\ \alpha_P + \alpha_U = 1 \end{aligned}$$

see [18] for details.

B.2.5 Solution procedure for the system

It is now possible to describe the solution sequence for our system of equations. A transient solution procedure for the incompressible, but thermally expansible and electrically conducting flow can be summarized as follows:

1. Set up an initial conditions for all field values.

2. Start the calculation from the new time-step values.

3. Go through the SIMPLE loop until the tolerance for the pressure-velocity system is reached. For this stage, pressure and velocity fields are obtained.

4. Using the results from the previous step, solve the enthalpy equation in order to obtain the new temperature field.

5. Update the properties of the gas using the new temperature distribution.

6. Using the updated electric conductivity of the gas solve first the electric potential equation.

7. Solve the equations for the magnetic potential field using the new information about the electric potential field.

8. If the final time is not reached, return to step 2.